Detecting the Surface Spin Polarization State of Topological Materials by Using Resonant X-ray Reflectometry

by

Rantong Gong

A thesis
presented to the University of Waterloo
in fulfillment of the
thesis requirement for the degree of
Master of Science
in
Physics (Nanotechnology)

Waterloo, Ontario, Canada, 2019

Author Declaration

I hereby declare that I am the sole author of this thesis. This is a true copy of the thesis, including any required final revisions, as accepted by my examiners.

I understand that my thesis may be made electronically available to the public.

Abstract

The topological insulator as a promising and low cost next generation spintronic device attracts lots of attentions recently. The spin-momentum locking is a characteristic feature of topological materials at the surface states. One consequence of spin-momentum locking is that a current induces a non-equilibrium spin polarization on the surface of a topological insulator. In turn, this spin-polarization can be used to manipulate the magnetization of materials that are in proximity to the surface of a topological insulator. Notably, the spin-orbit torque caused by topological material has a relative low cost of current, compared with heavy metals. Resonant X-ray Reflectometry (RXR) is used to probe this phenomena in a multilayer thin film comprised of a 3D topological insulator slab in contact with a soft magnet. By measuring x-ray reflectivity at several element edges using circularly polarized light, the polarized spin states near the interface between topological insulator and magnet are able to be probed, hence the current induced spin polarization of topological insulator surface states could be potentially determined.

Acknowledgements

I would like to frst thank my supervisor David Hawthorn for the opportunity he gave me to lead these projects. He spent many long hours with me at the experimental beamline, and he was always happy to help me, whether improving a measurement, improving a presentation, or encouraging me to try something difficult. Without a doubt, he is a great mentor and teacher to me.

I would also like to thank all the people who, at various times, have participated in the experiments themselves: Feizhou He (beamline scientist) and Ronny Sutarto (research associate), who have both gone beyond the call of duty too many times to recall, Namman Kumar Gupta and Christopher McMahon, my lab mates, who have both felt the chill of Saskatoon in the winter and know the joy of spending 4 hours to align the sample, He Ren, who makes a great contribution in growth of the thin films and helps me accomplish the sample fabrication.

Finally, I would also like to thank all of the people who have had an indirect, but important impact on the success of my research, either through discussions, hands-on training or friendship.

Table of Contents

List of Figures

Chapter 1

Introduction

1.1 3D topological insulator

Topological insulators (TIs) are novel electronic materials. Like ordinary insulators, they have a large bandgap in the bulk part. However, unlike the ordinary insulators, they have a protected conductive state on their edges or surfaces, which is a result of the combination of spin-orbit coupling and time reversal symmetry. The quantum spin Hall insulator states has been first studied in three dimensions in 2006 [12], and then it has been proved on several $Bi_{1-x}Sb_x$ materials [13]. At the surface states of these 3D topological materials, there is a result of strong Spin-Orbit Interaction (SOI), called Rashba effect, which can induce the spin polarization spontaneously without external magnetic fields [27, 14]. Surface states are forced with a perpendicular electric field because of the break of inversion symmetry. Due to this effective magnetic field caused by the gradient of perpendicular electric potential, the energy level (E) of electrons depends both on the direction of spins and the electron momentum (κ), leading to a spontaneous magnetization. The resulting spin polarized band dispersions are expressed as

$$E(\boldsymbol{\kappa}) = E_0(\boldsymbol{\kappa}) \pm \alpha \times |\boldsymbol{\kappa}|, \tag{1.1}$$

where the first term is the energy state without the Rashba effect and the second term is the spin/momentum dependent energy shift. Correspondingly, the Hamiltonian is

$$\mathcal{H}_{SO} = \alpha(\boldsymbol{\kappa} \times \hat{\mathbf{z}}) \cdot \boldsymbol{\sigma}, \tag{1.2}$$

where σ is Pauli matrix and $\hat{\mathbf{z}}$ is a unit vector perpendicular to the layer surface. A diagram illustrating this interaction is shown in Fig.1.1 (a). When an external current is passing through the TI surface, the edge states lacking inversion symmetry will generate a net spin accumulation, which is a result of uneven occupation of $\pm$ states under a presence of current [14, 7, 32, 41] (see in Fig.1.1 (b)). Therefore, there is an effective field acting on the imbalanced spin density of conduction electrons, and this field turns out to be critical for Spin Orbit Torque (SOT) in magnetic materials, which will be discussed further in section 1.2.1 [14, 2, 17, 35, 46].

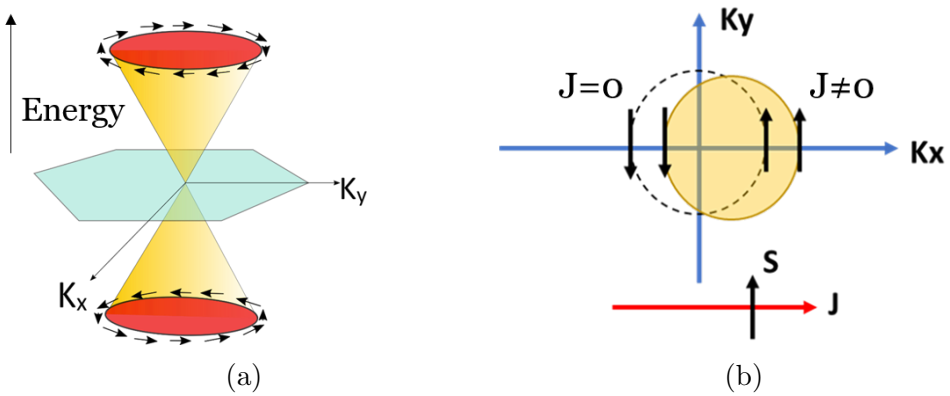

(a) (b)

Figure 1.1: Spin-Orbit Interaction (SOI) at topological insulator surface states. (a) In the simplest topological insulator the Fermi circle encloses a single Dirac point. (b) Top view of a slice in the $k_x - k_y$ plane of the TI surface states. An applied current generates a net momentum along k_x and spin-momentum locking gives rise to a net spin polarization oriented in-plane and at right angles to the current.

1.2 Motivation

1.2.1 Spin Orbit Torque (SOT)

The origin of magnetization manipulation with current injection can be traced back to the work of Slonczewski in 1996 [14]. This achievement required a physical principle called Spin Transfer Torque (STT), which required a flow of current passing between magnetic structures in order to transfer spin angular momentum. Usually the two magnetic layers are separated with a junction, which can be made by domain walls, nonmagnetic metal or

insulator (ie. DWs, tunnel junction, spin valve). Typically the current limit to trigger the effect is around $10^7 \mathrm{A{\cdot}cm^{-2}}$.

However, recently there is another way to achieve the purpose of magnetization switch with electric current, called spin-orbit torque (SOT). Although both of them are related to spin polarization, the modified spin-orbit torque originates from a different mechanism. As mentioned above in section 1.1, there is a strong interaction between spin and orbit in TI materials, and an in-plane current could induce TI surface state to be spin polarized. This current induced effect could be used to exert a torque on the magnetization of an adjacent magnetic layer in contact with TI channel by absorbing the polarized spin components that are perpendicular to the interface between magnetic layer and TI (see in Fig.1.2) [14, 19]. In addition, because of this strong spin orbit interaction of TI materials, the requirement of the amount of injected current to achieve the magnetization switch is 10 order of magnitude smaller compared with ultrathin heavy thin film metal [17], such as Au [22], which saves the current cost effectively.

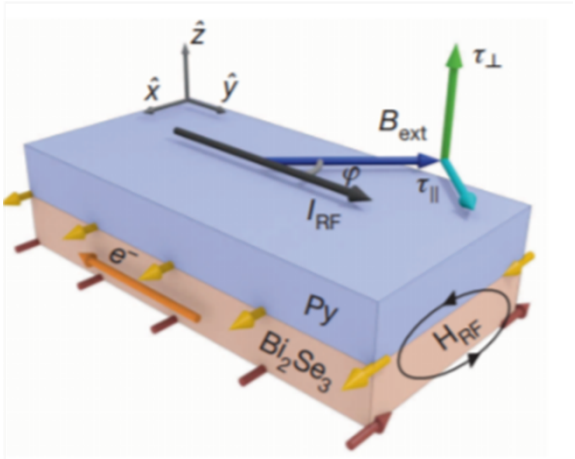

Figure 1.2: Strong spin-orbit interaction of TI exerts SOT on adjacent magnetic layer.

1.2.2 Previous studies of topological materials

The strong spin orbit interaction and promising future application of TI have attracted a lot of attention in vast range of experimental studies, which is well beyond the scope of this thesis. In order to understand the scale of this work, I will provide a short, but not complete, sampling of the various methods used to study these phenomena.

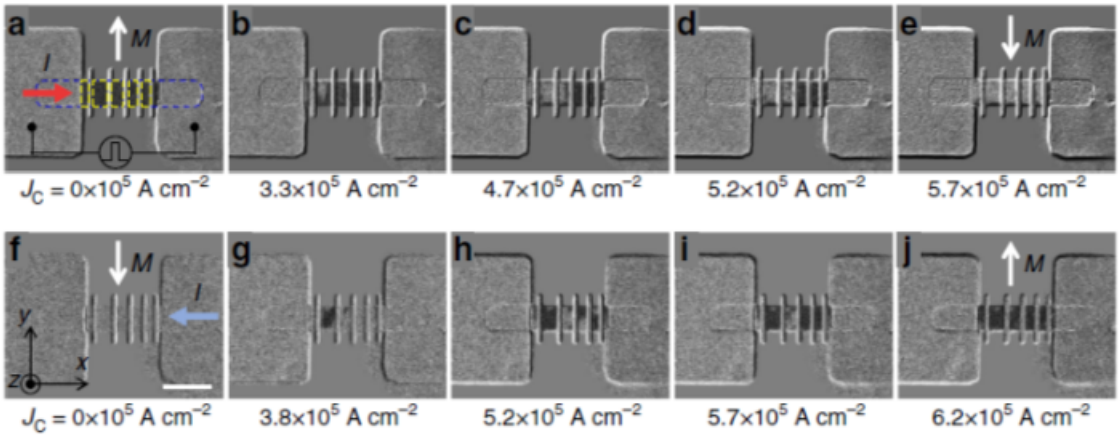

Figure 1.3: MOKE images of SOT-driven magnetization switching in Bi_2Se_3/Py without magnetic field at room temperature. From (a) to (e), MOKE images of magnetization switching by a pulsed dc current I along the +x-axis with increasing the current density J_C in the Bi_2Se_3/Py thin film denoted underneath the corresponding image. The blue dashed rectangle in a represents the 12 μm wide Bi_2Se_3/Py channel connected with two big contact pads. The yellow dashed boxes in a denote five small Py rectangles magnetically isolated by Cu bars. From (f) to (j), MOKE images of magnetization switching for an opposite I direction. The dark (light) contrast shows the magnetization along +y (y)-axis. The direction of magnetization is also indicated by the white arrows. Data comes from Ref. [44]

Several experiment techniques have been applied to explore the merit charge spin conversion of SOT, including Kerr effect measurement [14, 44] by using optical method to observe the magnetization switching, spin torque ferromagnetic resonance [43] to study the Spin Hall effect, and spin valve tunneling junction measurement [30] to illustrate the spin polarization efficiency of TI thickness dependence. These experiment attempts provide valuable evidence and reference to help us built the scheme of spin orbit torque measurement.

For instance, in Ref. [44] they demonstrate the SOT-induced magnetization switching in $Bi_2Se_3\,(8nm)/Py\,(6nm)$ bilayer heterostructure at room temperature with a pulsed dc current I. The soft magnetic anisotropy in the device is along the $\pm$y-axis (Fig.1.3 (a), (f)). This enables to observe the magnetization switching after pulsed dc current is off. For the MOKE imaging measurements, they first saturate the Py magnetization along the +y or y-axis with an in-plane external magnetic field H, then they remove H and

apply a pulsed dc current (500 s pulse width) to observe the magnetization switching using MOKE microscope. The current density required for the room temperature SOT-induced magnetization switching in Bi_2Se_3/Py is extremely low at $6 \times 10^5 \mathrm{A{\cdot}cm^{-2}}$, which is one to two orders of magnitude smaller than that with heavy metals [36, 10, 31]

Besides the SOT study, other features of topological insulators have been characterized in various aspects: the optical properties [52], quantum hall effect [38], thermal conductivity [23]. There has also been a great amount of experiment contributions in studying TI electrical surface-bulk structure and crystal growth properties.

1.2.3 A new method to study spin surface state of TIs: Resonant X-ray Reflectometry (RXR)

Though abundant methods have been used to study spin polarization and spin-orbit torque, there is still an unresolved question about spacial spin environment for multilayer stuctures. Regarding this question, new instruments for resonant soft x-ray reflectivity (RSXR) at low temperatures were developed. Reflectivity is given by interference of X-ray that are reflected by different interfaces, which is defined as a region of space with optical property change. In other words, reflectivity provides the information about structure properties of heterostructures, such as layer thickness [53]. Resonant reflectometry refers to x-ray reflectivity measurements with a photon energy that corresponds to an x-ray absorption edge [18]. Compared with off resonance, which is related to the total electron density, reflectivity at an absorption edge causes a core electron to transit into a higher energy unoccupied state before decaying back to the ground state. This resonant process greatly enhances the sensitivity of the scattering to particular electrons, providing element specificity as well as sensitivity to valence state and spin and orbital orientation. More details are given in Chapter 2. The so-called 'soft' x-rays correspond to lower photon energies (e.g., 100 to 2000 eV) and shorter penetration lengths than 'hard' x-rays (greater than 10 keV). Soft X-ray is critical for the study of SOT at the interface between TI materials and soft magnetic alloy because this energy range involves the element absorption edges, such as Sb M edge, Fe L edge, and Co L edge [40]. As a result of reflectivity measurement with photon energy dependence, the electronic structure can be mapped.

Chapter 2

Resonant X-ray Reflectometry

2.1 Overview

Resonant x-ray reflectometry (RXS) is a technique that extends conventional x-ray reflectivity (XR) beyond the study of atomic positions in order to gain element selective spin degree information about states of matter. This specificity is achieved by tuning the photon energy to an x-ray absorption edge, providing sufficient energy to excite an inner-shell core electron into an empty valence state such that it depends strongly on photon energy, photon polarization and the electronic environment of the reflectivity. This resonant effect enhances the reflection amplitude, making it possible to detect a wealth of information about the charge and spin degrees of freedom of the electronic order into the reflectivity process. In TI and soft magnet bilayer heterostructure, most of the interesting physics occurs at magnetic element edges near buried interface. These magnetic element states can be probed using soft x-rays which can resonantly excite the strong 2p $\rightarrow$ 3d core electron transition. In contrast, hard x-rays can only probe the 4p states well above the Fermi energy via the 1s $\rightarrow$ 4p transition.

Thanks to the development of the third generation synchrotrons, accurate and control of photon energy and photon polarization [8] are allowed with a better energy resolution (0.1eV, at E=1000eV) and improved x-ray beam focusing properties [3]. Moreover, the impact and importance of RXR has grown significantly thanks to numerous advances in instrumentation and the theory of the resonant reflectometry [1, 34].

In this chapter, fundamental aspects of RXR will be presented. A theoretical treatment tailored to supplement the following chapters is presented in section 2.2. Experimental

details particular to the REIXS beamline at the Canadian Light Source (CLS) will be discussed in section 2.3.

2.2 Fundamental mechanism of resonant X-ray reflectivity

2.2.1 Index of refraction and resonant X-ray reflectivity

Modern growth techniques allow materials to be designed and fabricated at the atomic or molecular level in order to make materials with desired physical properties. To physically understand these kinds of samples, a non-destructive method is required to characterize the internal interface properties. X-ray reflectivity turns out to be an excellent tool for this task, since the contrast in the index of refraction between the two materials gives rise to reflectivity.

Since X-ray is an electromagnetic wave, one should expect some kind of refraction phenomena at interfaces between different media. To describe such refractive phenomena, the media of interest are taken to be homogeneous with sharp boundaries between them, each having its own refractive index n[26]. In general, it can be expressed as

$$n = 1 - \sigma + i\beta \tag{2.1}$$

In a medium of uniform refractive index, of infinite extent, there is no reflection. Reflection arises from variations in the optical property, within a material or at its boundary with another material. When an incident electromagnetic wave approaches a boundary with different refractive index, the relation between the refract and incident wave is determined by the Snell's law, (see in figure 2.1)

$$cos\alpha = ncos\alpha' \tag{2.2}$$

According to this rule of wave propagation, the Fresnel equations characterizing the portion of the reflection is calculated as

$$r = \frac{a_r}{a_i} = \frac{\alpha - \alpha'}{\alpha - \alpha'} \tag{2.3}$$

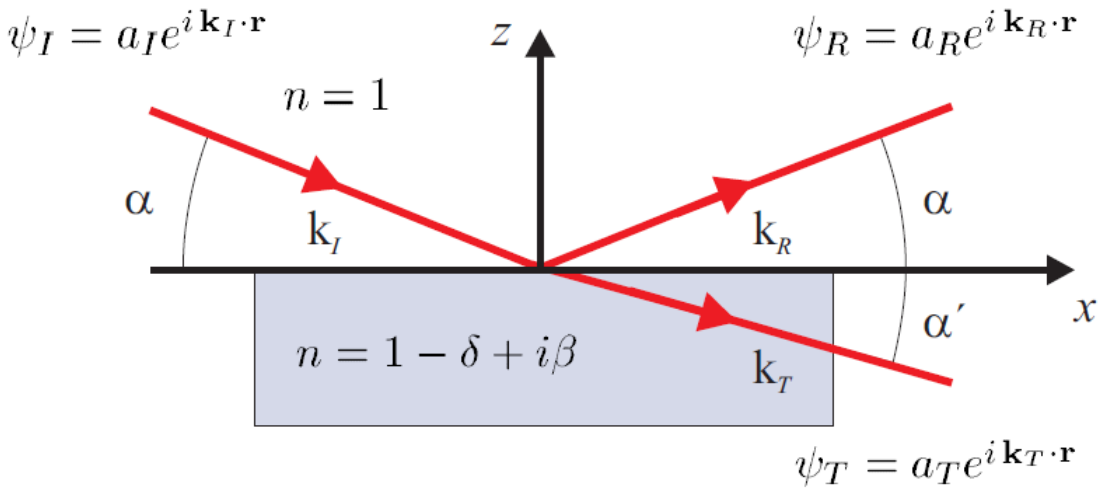

Figure 2.1: Snells law and the Fresnel equations can be derived by requiring continuity at the interface of the wave and its derivative.Ref. [1]

Based on these relations, reflectivity of an known incident X-ray wave and interfaces can be calculated to study the experimental results. For instance, the reflection of a single layer on a substrate can be described as the interference of the reflection at two interfaces. It requires the solution of the Fresnel equations for reflection and transmission and a phase-adjusted superposition including multiple scattering [49]. By calculating the reflectivity based on Snell's law, the reflectivity of a single layer deposited on a semi-infinite substrate is given by

$$R = |r_{slab}|^2 = \left| \frac{r_1 + r_2 e^{i2\boldsymbol{\kappa}\sin\theta d}}{1 + r_1 r_2 e^{i2\boldsymbol{\kappa}\sin\theta d}} \right|^2 \tag{2.4}$$

where $r_{1,2}$ are the Fresnel reflectivity coefficients of the free surface and the substrate interface, and d is the layer thickness. In Fig.2.2, the intensity of reflectivity calculated by this equation has been represented, which displays oscillations known as Kiessig fringes due to the interference of waves reflected from the top and bottom interfaces.

In addition, if we consider the frequency dependence of refractive index from a standard wave equation,

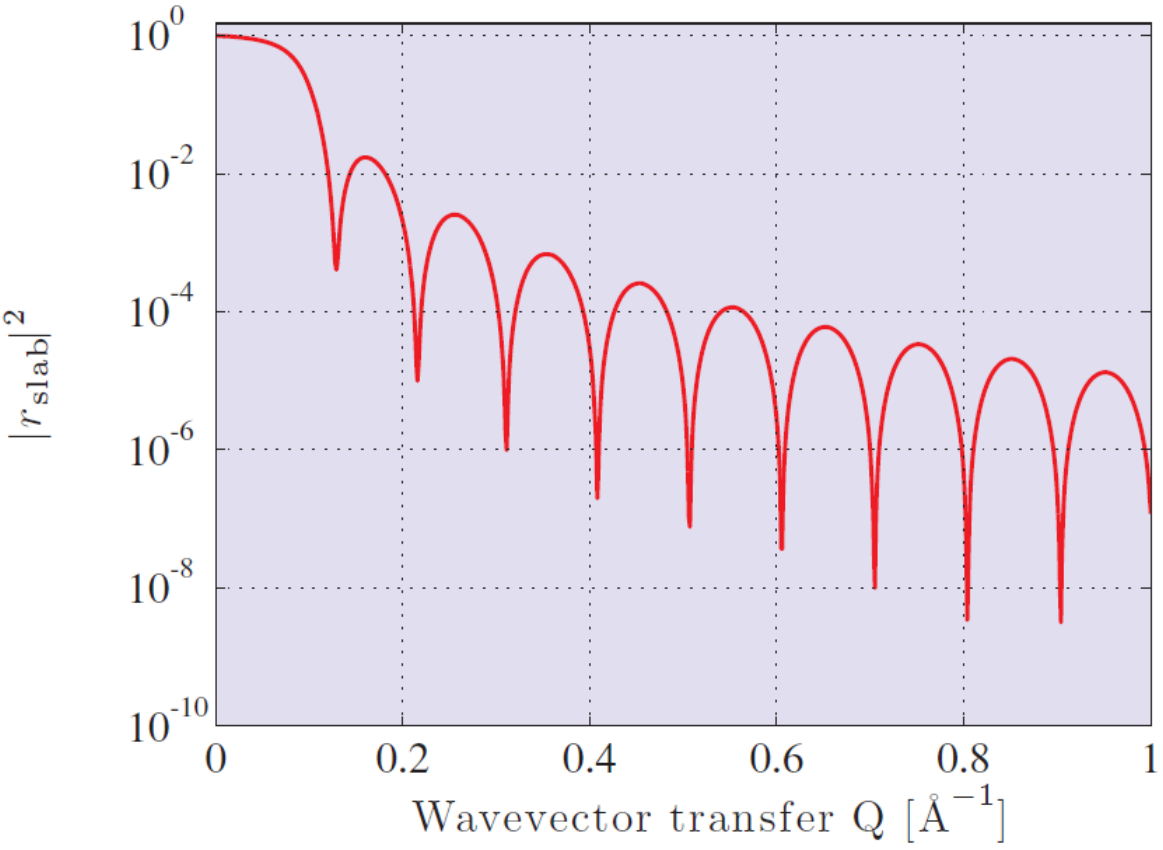

Figure 2.2: Kiessig fringes from a homogeneous slab of Tungsten. Solid curve: the calculated reflectivity $|r_{slab}|^2$ for a slab of thickness $10 \times 2\pi$ $\mathring{A}$. Ref. [1]

$$\left[\frac{\partial^2}{\partial t^2} - \frac{c^2}{n^2(\omega)}\right] E_T(\boldsymbol{r}, t) = 0\,, \tag{2.5}$$

the index of refraction can be also expressed in a Lorentz equation as

$$n(\omega) = 1 - \frac{1}{2}\frac{e^2 n_a}{\epsilon_0 m} \sum \frac{g_s}{(\omega^2 - \omega_s^2) + i\gamma\omega} \tag{2.6}$$

where the sum is taken over all distinct atoms, and n_a is the average density of atoms. From this expression, the refractive index n(ω) has a strong frequency dependence, particularly near the resonant frequencies ω_s. As it appears in Fig.2.3, there is a significant variation

of index of refraction when energy is at the vicinity of resonance. Hence, when the x-ray energy is tuned to an absorption resonance edge, within the same material, spatial regions containing elements at resonance will have optical properties very different from regions without resonating sites. In this situation, resonant X-ray reflectivity (RXR) gains critical sensitivity of electronic properties in an element specific way.

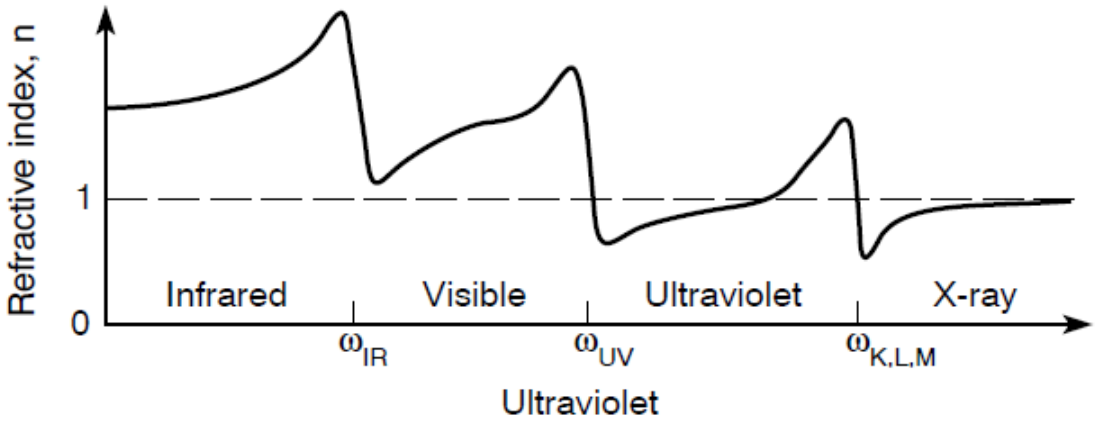

Figure 2.3: A sketch of refractive index showing the strong variations near IR, UV, and x-ray resonances (ω_s), and the general tendency toward unity for very short wavelengths where the frequencies are higher than all atomic resonances. Only the real part of the refractive index is shown here. Ref. [34]

Since the index of refraction is the sum of forward-scattered radiation from all atoms that interferes with the incident wave to produce a modified propagating wave, compared to that in vacuum, it should be a complex quantity involving both elastic and inelastic processes, which can be expressed in

$$n(\omega) = 1 - \frac{n_a r_e \lambda^2}{2\pi}\left[f^0(\omega)\right] = 1 - \frac{n_a r_e \lambda^2}{2\pi}\left[f_1^0(\omega) - i f_2^0(\omega)\right] \tag{2.7}$$

where r_e is the classical electron radius,

$$r_e = \frac{e^2}{4\pi\epsilon_0 m c^2} \tag{2.8}$$

and f^0 is complex atomic scattering factor. Since the refractive index can also been written in a simplified version as Eq. 2.1, the refraction and the absorption term σ and β will be written in the form of

$$\sigma = \frac{n_a r_e \lambda^2}{2\pi} f_1^0(\omega) \tag{2.9}$$

$$\beta = \frac{n_a r_e \lambda^2}{2\pi} f_2^0(\omega) \tag{2.10}$$

When the X-ray measurement is on resonance, both real and imaginary part of refractive index varies significantly implying the certain electron transition process during the measurement. For instance in Fig.2.4 (a), when the photon energy is approaching to 11567.5eV, the X-ray absorption represents a maximum peak, and this peak vanished at energies more than 30eV below and above. Correspondingly, variations in the dispersion (σ) and absorption (β) coefficient of index of refraction is huge around this energy value and almost disappeared beyond the energy range. What causes this maximum absorption is closely related with Pt electronic structure, where core electron occupied at $2p_{3/2}$ state is excited to an empty 3d state appeared in Fig.2.4 (b), also referred to as Pt L_3 edge.

In conclusion, the Resonance X-ray reflectivity is able to probe and capture both the spacial geometry and electronic structure of the material, which turns out to be a great tool to study interfaces property of a herterostructure material.

2.2.2 Polarization dependence of RXR

Resonant X-ray reflectometry not only provides the electronic structure of materials but also gives information on their magnetic states. For a magnetized material, the valance state such as d shell has a spin moment which is given by the imbalance of spin-up and spin-down electrons or equivalently by the imbalance of spin-up and spin-down holes [39, 42, 6](see in Fig.2.5). In order to measure the difference in the number of d holes with up and down spin, we need to make the x-ray absorption process spin dependent. This is done by the use of right or left circularly polarized photons which transfer their angular momentum to the excited photoelectron.

The photoelectron carries the transferred angular momentum as a spin. If the photoelectron originates from a spin-orbit split level, for example the $p_{3/2}$ level (L_3 edge), the angular momentum of the photon can be transferred partially to the spin through the spin-orbit coupling. Right circular photons (RCP) transfers the opposite momentum to the

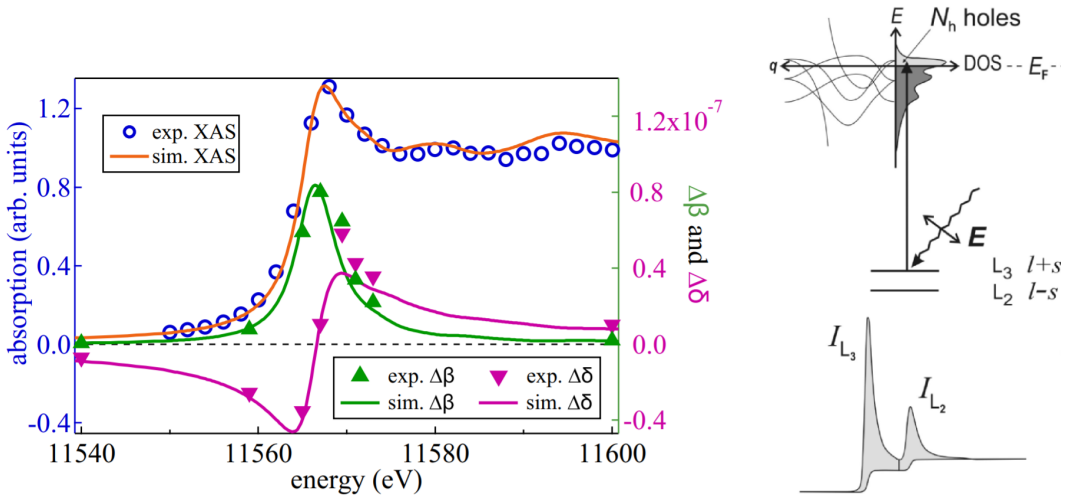

(a) (b)

Figure 2.4: Electronic information capture by X-ray absorption (a) Energy dependent XAS spectra and corresponding optical parameters σ and β at Pt L_3 edge. Experimental data are from Ref.[28]; (b) Scheme of an electron transition ($2p \rightarrow 3d$) process and corresponding spectra.

electron as left circular photons (LCP) photons, and hence photoelectrons with opposite spins are created in the two cases. Since the $p_{3/2}$ (L_3) and $p_{1/2}$ (L_2) levels have opposite spin-orbit coupling, the spin polarization will be opposite at the two edges.

As an example shown in Fig.2.5, the dichroism signal ($I_{RCP} - I_{LCP}$) at the L_3 and L_2 edges are identical in magnitude but of opposite sign. At the L_3 edge, X-rays with polarized photons which have positive angular momentum excite more spin-up electrons than X-rays with polarized photons which have negative angular momentum, and at the L_2 edge the opposite is found. It is easy to show that for the calculation of the dichroism effect it is equivalent to fix the X-ray spin and switch the magnetization direction [37]. In principle, L-edge X-ray absorption spectra contain contributions from both p $\rightarrow$ d and p $\rightarrow$ s transitions, but in practice the p $\rightarrow$ d channel dominates significantly. [9]

While X-ray Magnetic Circular Dichroism (XMCD) only gives the mean polarization of the magnetic thin film, x-ray resonant magnetic reflectivity is directly sensitive to the spin polarization at the interface. The magnetic dichroism for circularly polarized light reflected by the spin polarized interface results in a slightly different x-ray reflectivity for varying magnetization directions due to a change of the optical constants of the spin

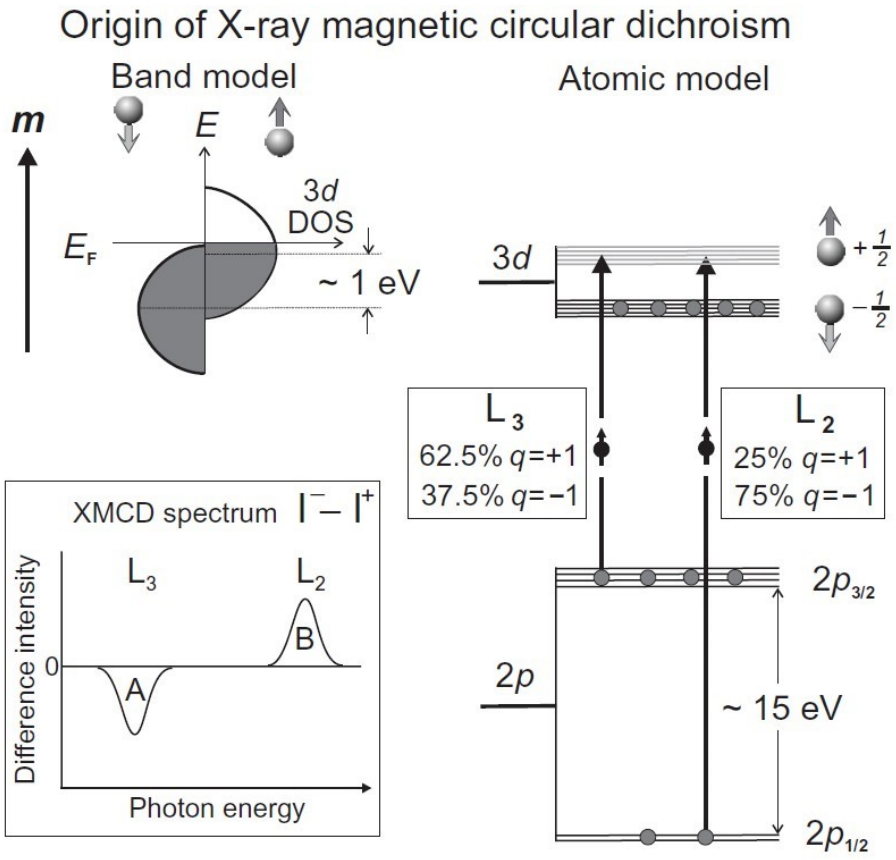

Figure 2.5: Illustration of the L edge X-ray absorption processes of circularly polarized photons with angular momentum q = ±1. The magnetization direction has been determined such that the down-spins are filled and the up-spins partially unfilled. In the atomic model, the possible 2p core to 3d valence transitions has been illustrated with respect to circularly polarized light with different angular momentum q. The fraction of up-spin electrons excited from the p core shell through absorption of X-rays with angular momentum q = ±1 is listed for the L_3 and L_2 edges. Here, the X-rays is assumed to incident parallel to the atomic magnetic moment m. Ref. [40]

polarized material. From Fig.2.6 (a) magnetic resonant reflection of the (Ga,Mn)As film as a function of angle with the photon energy at the peak of the L_3 absorption edge (E=639.5 eV). Above T_C, the sample is paramagnetic and the measurements with left and right circularly polarized light overlap well. The observed Kiessig fringes correspond to

the 45 nm thickness $Ga_{0.93}Mn_{0.07}As$ layer. Below T_C, significant dichroism is seen in the reflectivity. In Fig.2.6 (b) the measurements of x-ray absorption and x-ray reflectivity at a fixed angle, along with the dichroism for each measurement. By combining reflectivity verses angle and photon energy, a spatial magnetization environment of this layered sample could be profiled.

2.3 Experiment beam design

2.3.1 Beamline

The RSXR experiments presented in this thesis were all performed at the Canadian Light Source's Resonant Elastic and Inelastic X-ray Scattering (REIXS) 10ID-2 beamline with an in-vacuum four-circle diffractometer [21]. The insertion deviec (ID) at REIXS is an elliptically polarizing undulator (EPU) including 43 poles having a 75 mm period and spanning 1.6 m. This EPU can produce linearly polarized photons with an energy range 100-3000eV or circularly polarized (left or right) photons with 100-1000 eV.

The optical configuration of the REIXS beamline is shown schematically in Fig.2.7. REIXS has a variable line spacing plane grating monochromator with three gratings (Ni low energy, Au low energy, Au high energy) and four coatings (Ni, C, Si, Au) on the plane mirror. These can be chosen to optimize flux at photon energies spanning the full energy range of the beamline. A variable exit slit can be used to adjust energy resolution. The size of the exit slit gap is typically set in the 10 to 50 m range and is approximately proportional to flux. The beam spot size at the sample position is width x height =300 x150 μm^2.

The entire beamline is operated in an ultra-high vacuum (UHV) environment (P $<$ 10^{-9} Torr). There is a need to ensure a long life of the electronic track in the storage ring. This is also important for the use of soft X-rays, because even with moderate pressure, the average path length of soft X-rays is still severely affected. UHV operation also reduces the amount of contaminants that may be generated on the optical components. By limiting the adsorption of gases such as water vapor or potentially condensing the beam lines onto these components. This is also very significant for samples requiring heating and cooling process in a vacuum because these measurements (eg, electron yield or resonance reflectance) may be sensitive to the surface condition of the sample.

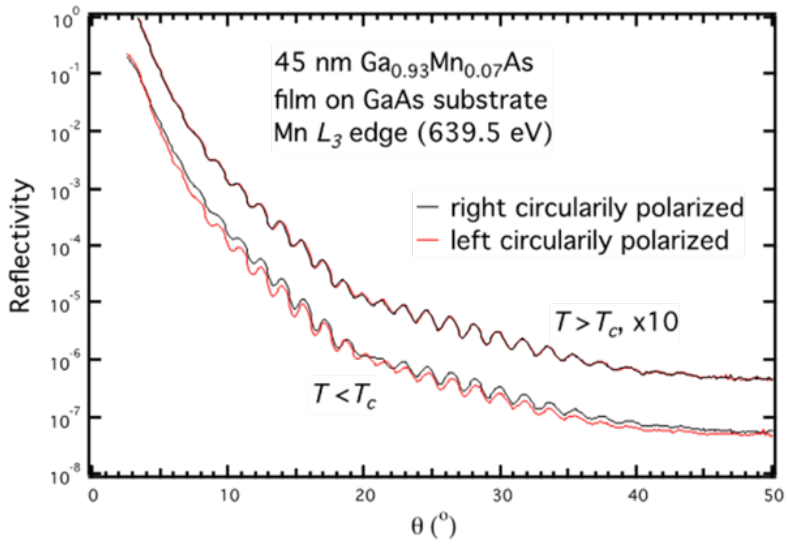

(a)

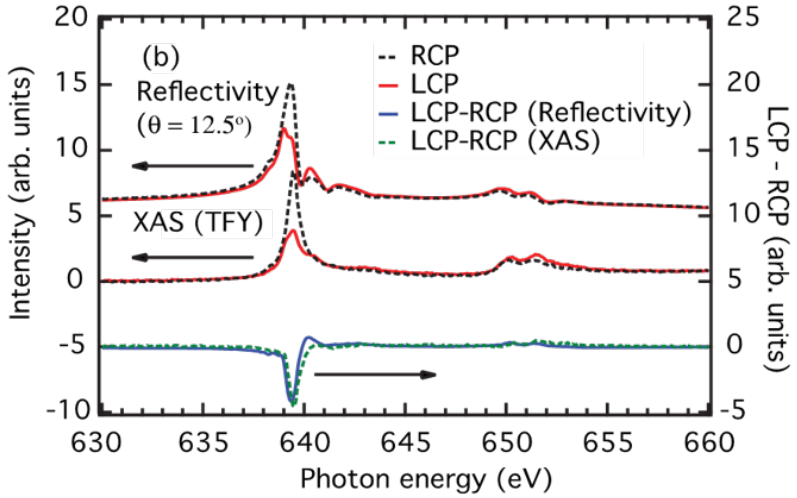

(b)

Figure 2.6: Magnetic resonant reflectivity measurements at the Mn L edge of a thin film of Ga0.93Mn0.07As on a GaAs substrate. (a) Reflectivity with varying angle of incidence measured at the L3 edge with left and right circularly polarized photon. The sample is measured both above and below the Curie temperature, with a dichroism observed only in the ferromagnetic state. (b) Reflectivity with θ at 12.5° and x-ray absorption as a function of photon energy. The dichroism of both the reflectivity and XAS have similar lineshapes. Experimental data are from Ref.[20]

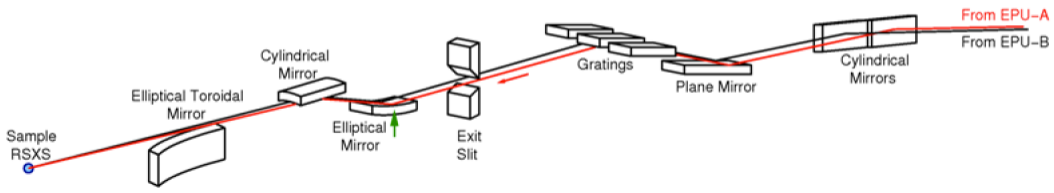

Figure 2.7: Schematic of REIXS beamline showing novel x-ray optics configuration capable of sending spatially separated beams from two EPUs to the sample position simultaneously.

2.3.2 Detection scheme

The following discussion is brief introduction of some of the essential aspects of the elastic scattering chamber and diffractometer design, which are covered thoroughly in Ref [21]. The 1 m diameter stainless steel vacuum chamber pictured in Fig.2.8 at the REIXS beamline houses an UHV 4-circle diffractometer (see in Fig.2.9) consisting of a 2-circle goniometer mounted on a central ring and a detector arm mounted on a separate 2-ring. The diffractometer is mounted on a separate subframe than the main scattering chamber and is connected to it with flexible bellows, so that the diffractometer can be translated into the x-ray beam path independent of the main scattering chamber.

A load lock is used so samples can be transferred without venting the scattering chamber. The load lock has a garage for storage of up to 3 sample holders at a time. Sample holders are transferred into the scattering chamber using a magnetically coupled rack and pinion linear translator that uses a pincer mechanism to securely hold onto a small tab on the sample holder. Gate valves are used to isolate the scattering chamber from the beamline and the load lock from the scattering chamber during sample transfers.

The load lock is pumped down with a 300 L/s Per turbopump and typically reaches 5×10^{-7} Torr in 45 minutes or less, sufficiently low for transfers. The main chamber is pumped using a 700 L/s Per turbopump (backedby a triscroll roughing pump) and a CTI Cryotorr 8F cryopump. A closed cycle cryostat is mounted on a differentially pumped rotatory feedthrough, located at the top of the chamber. The feedthrough is pumped in two stages by the triscroll pump and a 2 L/s ion pump. The pressure in the scattering chamber is usually better than 5×10^{-9} Torr. Pressure gauges include a cold cathode gauge, a hot lament ion gauge and a residual gas analyzer, for low pressure measurements, as well as thermocouple and convectron gauges for intermediate and high pressures, respectively.

Sample translations up to ± 7.5 mm are accomplished with stacked x, y and z linear

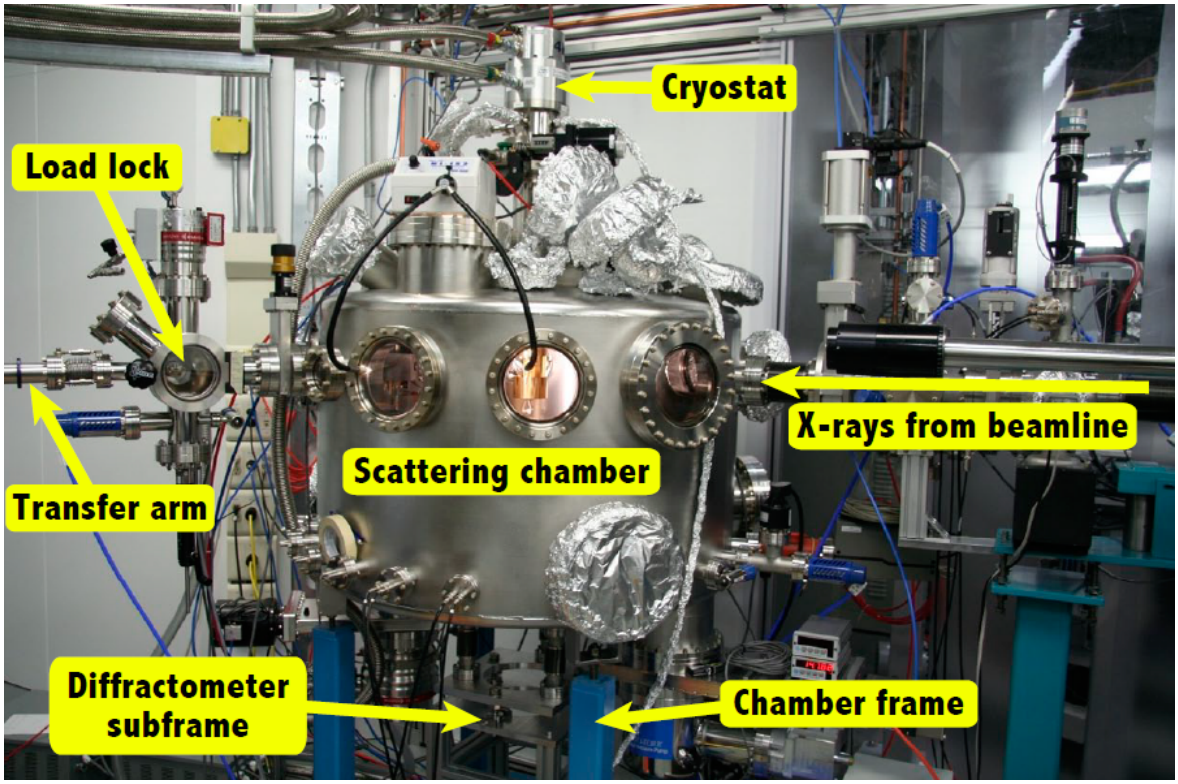

Figure 2.8: The RSXS scattering chamber at the CLS's REIXS beamline. A polarized monochromatic beam of soft x-rays from the beamline enter from the right and focus at the sample position, centred in the scattering chamber. A load lock is used to store samples and facilitate sample transfers. The closed-cycle cryostat is mounted on top of the scattering chamber.

translation stages mounted on the goniometer. The θ and 2θ motions,originally supported motion ranges of -25° to $+265^{\circ}$, but due to instrument adjustment and practical considerations, ranges of -60° to $+165^{\circ}$, for θ and -25° to $+172^{\circ}$, for 2θ are currently imposed.

Four detectors are currently installed on the detector arm (Fig.2.10): a micro-channel plate (MCP), a photodiode (PD), a channeltron (ChT) and a polarization analyzer. These are located at a radius of 29 cm from the sample position and are mounted to a structure that can be raised or lowered by 40 mm to place any of the detectors in the scattering plane. The MCP has a 25 mm diameter and provides 2D sensitive single-photon detection capability. A negatively charged grid is placed in front the MCP to capture positively charged ions (from ion gauges or possibly ejected from the sample). The front surface is

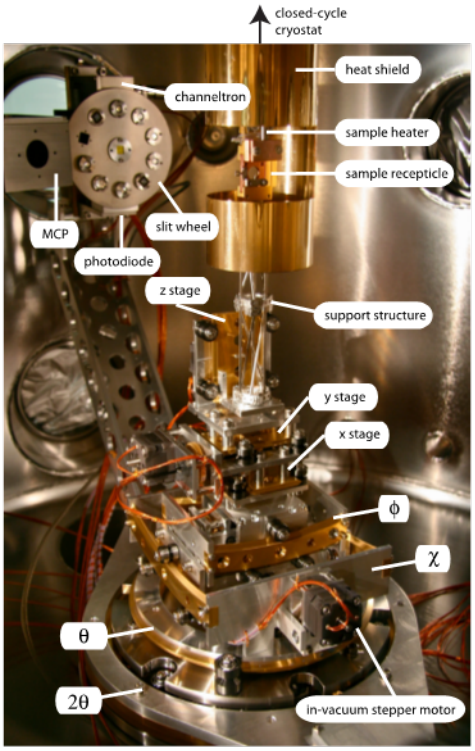

Figure 2.9: The in-vacuum four-circle diffractometer at the CLS's REIXS beamline.

also negatively biased to repel electrons from the surface. The ChT is a 10 x10 mm detector that provides single photon sensitivity similar to the MCP but without 2D sensitivity. It has a similar biasing scheme as the MCP. The PD has a 10 x10 mm active area, is sensitive to a very wide range of photon energies with a linear response for photon energies up to 5keV and a high dynamic range.

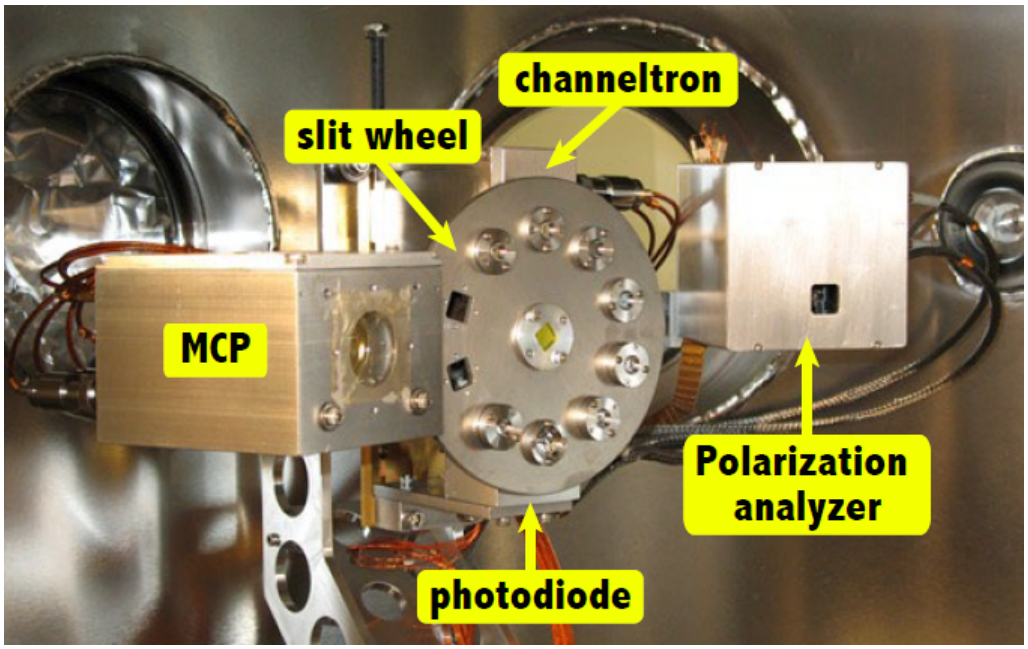

Figure 2.10: The in-vacuum four-circle diffractometer at the CLS's REIXS beamline.

Chapter 3

Materials and Sample Preparation

3.1 $(Bi0.5Sb0.5)_2Te_3/Co_{40}Fe_{40}B_{20}$ thin film

To generate a topological insulator, whose spin-orbit coupling must be strong enough to modify the electronic structure significantly, the heavy-element, small-bandgap semiconductors are the most promising candidates. This suggestion originates from tow reasons. First, spin-orbit coupling is a relativistic effect and is only strong for heavy elements. Second, if the bandgap is much larger than the energy scale of spinorbit coupling, then spin-orbit coupling will not be able to change the phase [21, 50]. Based on these assumptions, the $Bi_{1x}Sb_x$ as the first generation of 3D topological insulator has been studied by angle resolved photoemission spectroscopy (ARPES) technique [24, 25].

Since pure bismuth and pure antimony both have a finite direct band gap, their valence bands can be topologically classified. Pure bismuth is a semimetal with strong spin-orbit interactions. Its band structure, which is shown schematically in Fig.3.1 (a), has a feature of conduction and valence band overlap, leading to pockets of holes near the T point in the Brillouin zone and pockets of electrons near the three equivalent L points. The valence and conduction bands at the L point, derived from antisymmetric L_a and symmetric L_s orbitals, have a small energy gap. Substituting bismuth with antimony changes the critical energies of the band structure. As shown in Fig.3.1 (b), the band rearrangement can be observed with a doping level adjustment. Based on the experimental test, the band structure of this compound is varying with respect to the concentration of Sb. when an Sb concentration is too small, the top of the valence band at T moves below the bottom of the conduction band at L, and the material becomes an insulator. As x is increased to a large value, the valence band rises above the conduction band, restoring the semimetallic state. Between

them, there is a balance point, where gap between L_a and L_s closes and a truly massless 3D Dirac point is realized.

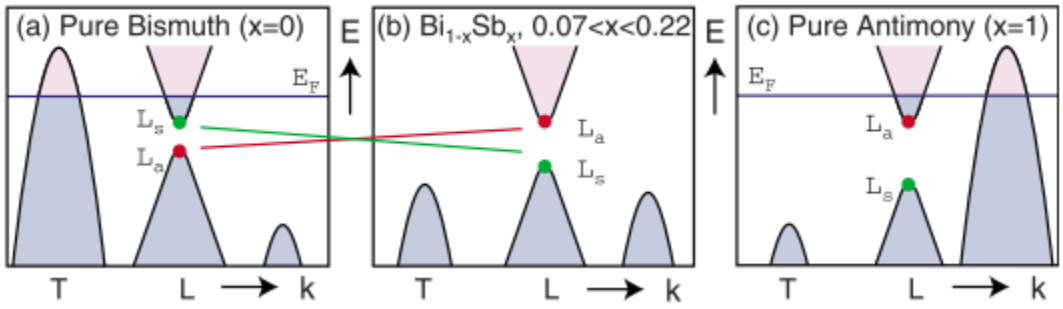

Figure 3.1: Schematic representation of the band structure of $Bi_{1x}Sb_x$. Ref. [19]

In addition, both transport and hysteresis properties benefit from the amorphous $Co_{40}Fe_{40}B_{20}$. $Co_{40}Fe_{40}B_{20}$ has a small resistance (20Ω) and quite soft magnetic properties, which has a low coercive field and high magnetic permeability. For a magnetic material, it cannot be fully magnetized until the magnetic field approaches the coercive field (H_C), and it is able to maintain the magnetization (M_R) when the field is removed, shown in Fig.3.2. Therefore, the soft magnetic properties allow the $Co_{40}Fe_{40}B_{20}$ to be easily magnetized and to keep the magnetization when the field is removed.

According to these ideas, $Co_{40}Fe_{40}B_{20}$/ $(Bi_{0.5}Sb_{0.5})_2Te_3$ bilayer thin film has been designed and generated. In my experiments, the $Co_{40}Fe_{40}B_{20}$/ $(Bi_{0.5}Sb_{0.5})_2Te_3$ thin films have been mainly studied and discussed. These thin films were grown by Molecular Beam Epitaxy (MBE) in Professor Guoxing Miao's lab. Thanks to his instruction of the material choice and his PhD student He Ren's hard work on sample synthesis, we can have this opportunity to study this kind of materials with unique and novel surface states.

3.2 Sample preparation

It is critical and essential to prepare samples as close as possible to the ideal situation. Unlike the hard X-ray, RXR measurement is highly sensitive to the surface quality and sample orientation. Moreover, according to the SOT condition, the sample has to be applied with sufficient current density in order to achieve the limit. In this section, I will illustrate and discuss the methods to prepare the sample in terms of sample wiring, fabrication and sample mounting.

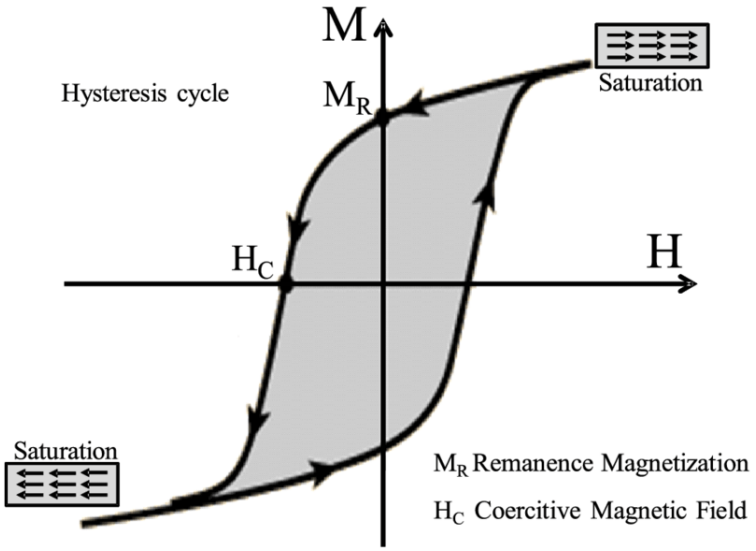

Figure 3.2: A plot of magnetization M against magnetic field H. Starting at the origin, the upward curve is the initial magnetization curve. The downward curve after saturation, along with the lower return curve, form the main loop. The intercepts H_C and M_R are the coercive magnetic field and remanence magnetization.

The design of the sample structure at the beginning is a multilayer thin film, consisting of Al_2O_3 (1nm)/ $Co_{40}Fe_{40}B_{20}$ (1.5nm)/ $(Bi_{0.5}Sb_{0.5})_2Te_3$ (5nm) sandwich distribution (see in 3.3 (a)). During the practical measurement, the 1nm capping layer Al_2O_3 was get rid of with the silicon knife cleaving. In order to make contacts with the current channel, the silver past was applied to connect between the thin film and 2μm thick copper wires, as shown in Fig.3.3 (b). Since sample thickness in total is only 7.5 nm, this operation of electrical connection has potential risks of the wire bumping and surface contamination. In addition, the current density applied in the Kerr effect measurement mentioned in previous section 1.2.2 with similar material composition is up to 10^5A·cm^{-2}, but in our experiment since the restriction of rectangular shape, current density only reach a maximum of 10^4A·cm^{-2}[44].

Based on experience from the initial measurement, a new design of sample shape pattern has been created (see in Fig.3.4).The pattern has two branches that are perpendicular with each other. As shown in in Fig.3.4 (b), When the current is applied to this device, one of the branches' spin current direction is parallel or antiparallel to the angular momentum of incident light, which is supposed to maximize the magnetic dichroism, and the other one's polarized spin direction is perpendicular to the beam. For each branch, there are three

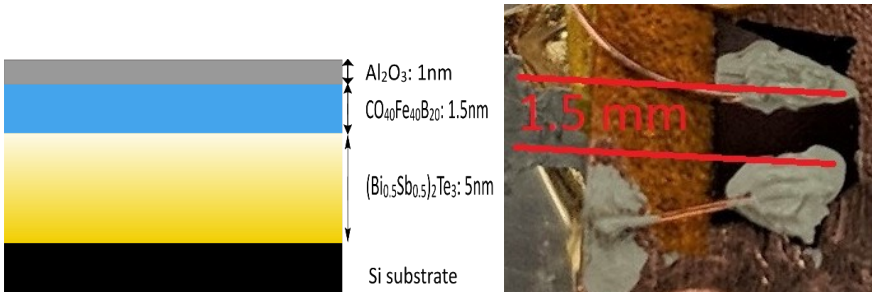

(a) (b)

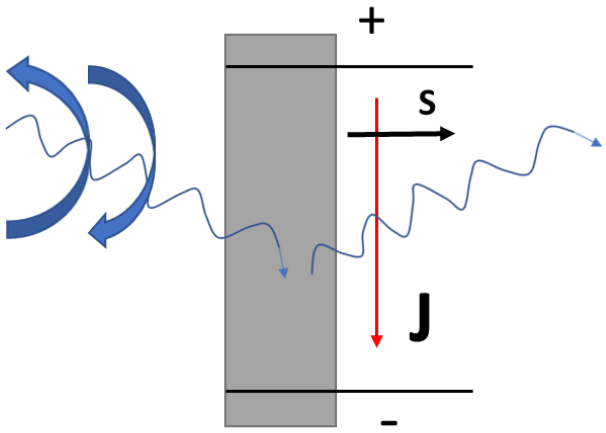

(c)

Figure 3.3: Geometry of the thin film and wiring situation. (a) Al_2O_3 (1nm)/ $Co_{40}Fe_{40}B_{20}$ (1.5nm)/ $(Bi_{0.5}Sb_{0.5})_2Te_3$ (5nm) grown on silicon (1 1 1) substrate by Molecular Beam Epitaxy (MBE). (b) This scheme represents the orthogonal orientation relation between in-plan current and incident beam (red and black arrow pointing the directions of charge movement and spin polarization respectively). (c) Silver past has performed to make electrical contacts in electrical circuit.

parts with different width (50μm, 100μm, and 2mm), so that reflectivity can be probed with different current densities by only moving the beam position without changing the bias voltage. At two ends of the pattern, there are two yellow squares representing the metallic electrodes.

To synthesis this new device, a nanofabrication process has been applied in the Uni-

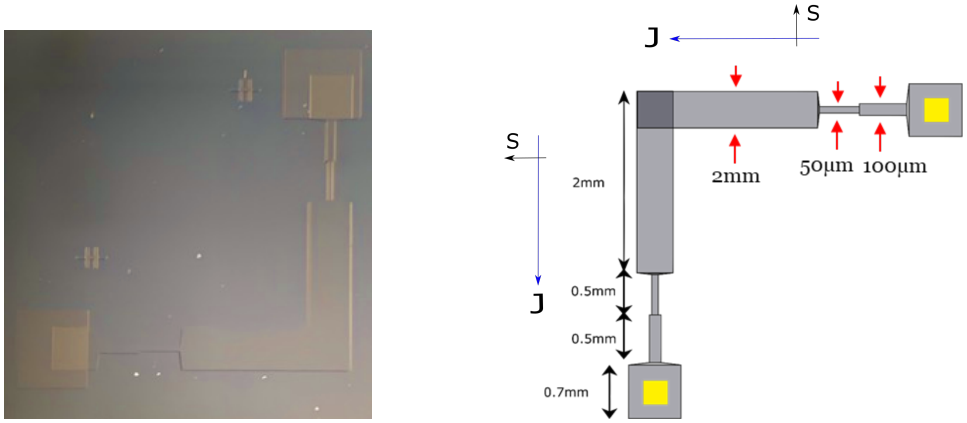

(a) (b)

Figure 3.4: Fabrication pattern design and result. (a) a result of fabrication on Al_2O_3 (3nm)/ $Co_{40}Fe_{40}B_{20}$ (3nm)/ $(Bi_{0.5}Sb_{0.5})_2Te_3$ (7nm)/ Sapphire. (b) Pattern was design in inverse L shape in order to measure the spin polarization in perpendicular and parallel orientation simultaneously by tuning beam positions.

versity of Waterloo NanoFab, shown in Fig.3.5. The device was covered with a 1000nm thick photoresist with the twin spin coater and patterned with a Maskless Aligner (MLA) photolithography of 405nm UV light when the does was $100mJ/cm^2$ and defocus was 0, which can be observed in Fig.3.5 step (1) and (2), following with a sequence of the Ar ion milling etch with 400V 190mA for 5 minutes by using the AJA ATC Ion Mill. Then, the capping layer of photoresist and Al_2O_3 were get rid of by a heat bath of Remover PG solvent and MF319 solution respectively. There was a second lithography and etching process to create the electrodes, which were simply repeated step (1) to (3). Two 100nm thick Au pads were directly deposited on the $Co_{40}Fe_{40}B_{20}$ surface with an Ebeam evaporator of Intlvac Nanochrome II-UHV system, (See in Fig.3.5 step (8) and (9)).

Finally, the whole piece of thin film was mounted on a copper sample plate with a kapton tape, which is used to insulate the Nd at the backside of the sample with copper plate. One end of the electrode is connected to ground through the sample plate. The other one connecting with electrode installed on the sample plate will have a contact with applied bias outside of chamber through the feedthrough. Fig.3.6 shows the circuit scheme during the experiment.

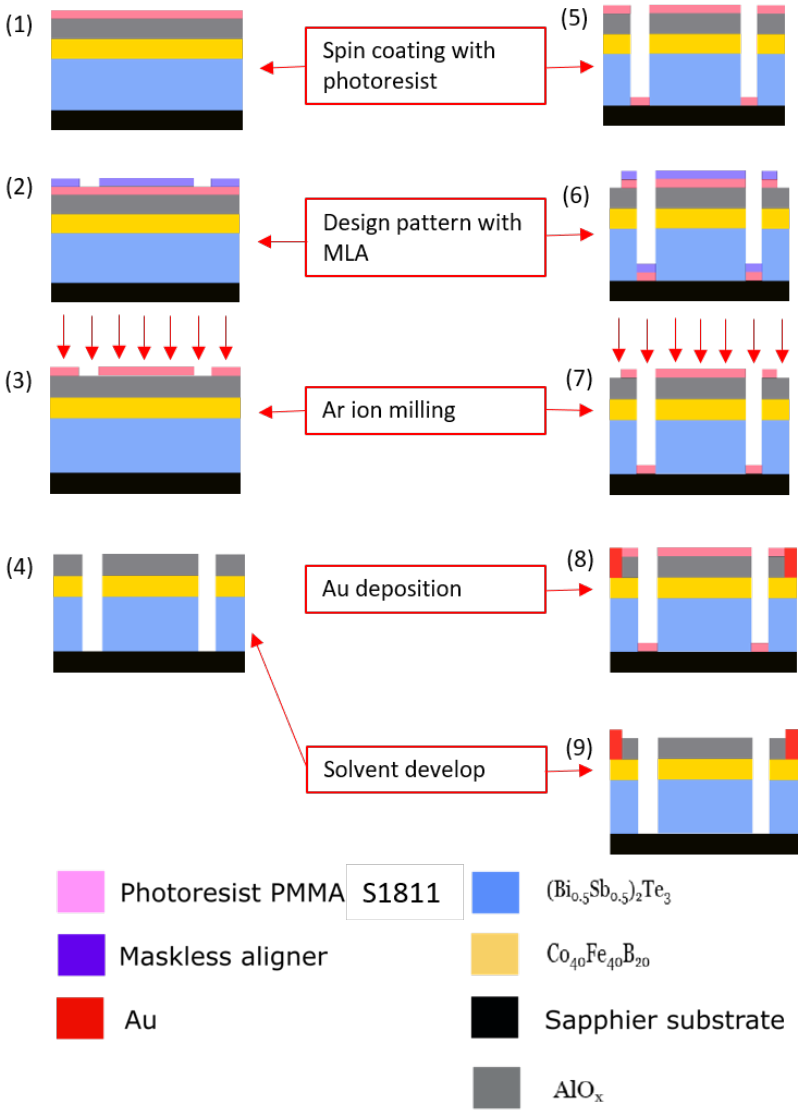

Figure 3.5: Nonafabrication procedure. photoresist emission mask PMMA S1811 has be applied during the lithography; Al_2O_3 develop solution is MF 319.

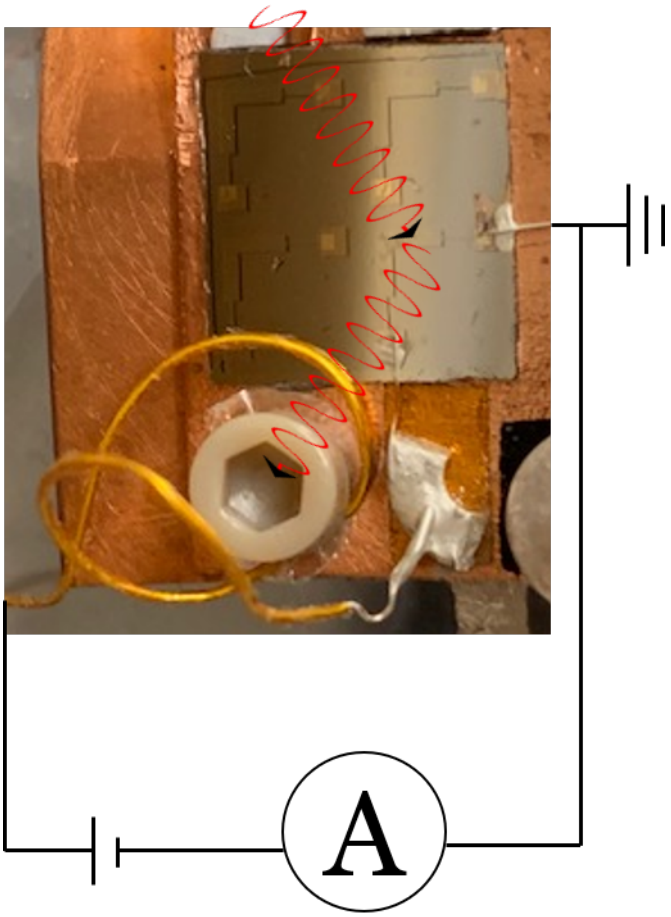

Figure 3.6: Overview of the sample mounting and a scheme of electrical circuit. Red arrows represent the incident and reflect beams.

Chapter 4

Reflectivity Measurement of Multilayer Thin Film: Al_2O_3/ $Co_{40}Fe_{40}B_{20}$/ $(Bi_{0.5}Sb_{0.5})_2Te_3$

4.1 Overview

Due to the promising future of spintronic and magnetic memory application mentioned in previous chapter, topological materials and soft magnet bilayer heterostructure has been studied in a wide range of experimental methods, such as optical Kerr measurement applied to observe the SOT induced magnetization [44], and angle-resolved photoemission spectroscopy (ARPES) performed for mapping the electronic band structure [51]. However, those measurement only capture the average spin state of the thin film. By contrast, the resonant X-ray refletivitometry allows us to probe the buried interface structures in a non-destructive way. Therefore, resonant x-ray reflectivity (RXR) is an ideal tool to study thin film herterostructure. In this chapter, the RXR measurement, with advanced synchrotron radiation, of the thin film Al_2O_3/ $Co_{40}Fe_{40}B_{20}$/ $(Bi_{0.5}Sb_{0.5})_2Te_3$ was performed under an in-plane magnetic field. Since the reflectivity measurement by synchrotron beamline is a relatively complicated system, some details of the measurement scheme will be discussed in section 4.2. Section 4.3 will present several results of RXR detected on several element edges which is discussed in section 4.4.

4.2 Reflectivity measurements

For all the RXR experiments discussed in this thesis, the reflected beam has been collected and analyzed with the photodiode detector mentioned in section 2.3.2. In order to receive reliable signals, the beam position has to be guaranteed on the same spot of the thin film surface, which is independent of the θ, ϕ, and χ adjustment. This requires both of the alignment of beam centering roughly by a telescope and the sample position centered by $\theta/2\theta$ scan with various angles. Moreover, as a result of thermal expansion, the sample position could shift when there is a large temperature change, such as cooling from 299K to 23K. To ensure where the beam spot is still on sample area, it requires extra alignments in position and angles. Fig.4.1 represents an instance of the alignment scheme.

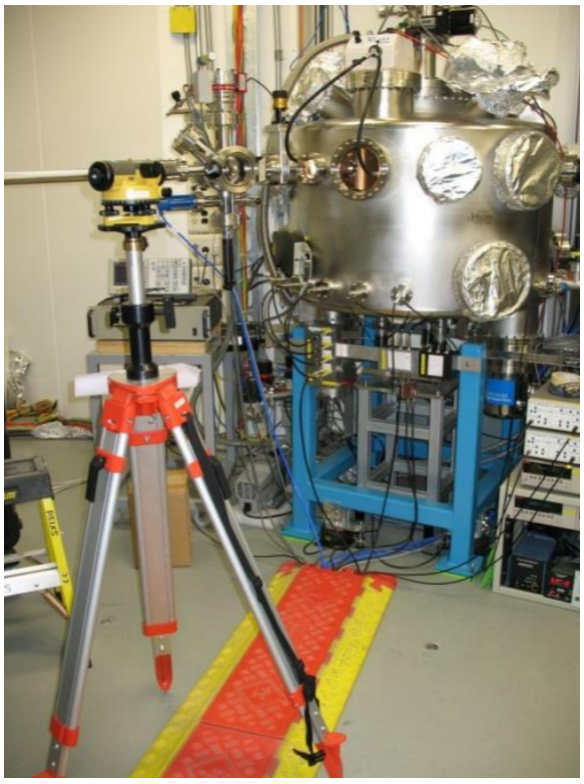

Figure 4.1: Incident beam is roughly aligned with a telescope through windows of UHV chamber

Based on the precise alignment results, resonant reflectivity of the thin film surface can be measured by tuning either the photon energy or incident angle with the other

variable fixed. During the measurement, a 0.6T magnetic field was applied horizontally and parallel to the sample surface using a Halbach permanent magnet array. Fig.4.2 presents a schematic relation between beam and magnetic field relative to the sample surface.

Additionally, since the thin film has been grown on a silicon substrate, the sample is electrically isolated from sample holder when there is no charge current. In order to collect the total electron yield (TEY) signal, which requires increasing conductivity between sample and sample holder, there is a piece of carbon type applied at the corner of sample surface.

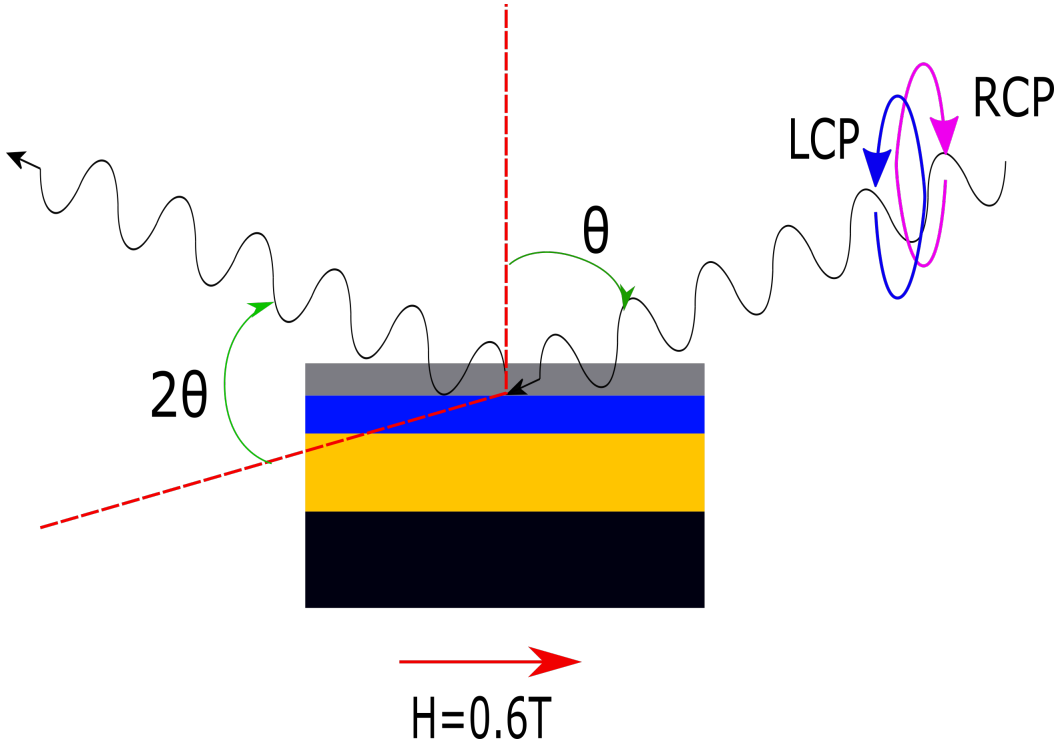

Figure 4.2: Reflectivity scheme illustrates the incident and reflect beam in θ and 2θ directions respectively, and external magnetic field is applied parallel to the film surface. θ is defined as the angle between the sample surface normal direction and the incident X-ray that is always parallel (anti-parallel) to the magnetic field direction (red arrow pointing direction). Purple and blue arrows represent circular right and left polarized light.

4.3 Results

Reflectivity was measured at several TI and magnetic element edges with circular left and right polarization light under a 0.6T in-plane magnetic field. According to different sensitivities of spin directions of polarized beam, the spin polarization could be observed with dichroism [40]. Fig.4.3 illustrates the reflectivity measurements at Sb M_5 edge. When θ is 20°, there is a reflectivity peak clearly illustrated at E=528eV (see in Fig.4.3 (a)). This photon energy, also known as Sb M_5 edge, corresponds to the Sb $3d_{5/2} \rightarrow 5p$ transition, probing the unoccupied 5p state [48]. On resonance, the reflectivities measured with respect to circular left and right polarization photons are almost identical, suggesting that there is no imbalanced spin population. Hence, spin states at TI surface have not been polarized. In addition, same overlap results has also been observed in Fig.4.3 (b) with an angle resolved reflectivity measurement. The oscillating peaks at varying angles correspond to the reflection interference at different atomic surfaces, which gives rise to no spin polarization at interfaces. To conclude, these RXR measurements provide evidence that there was no induced spin polarization at TI surface when a magnetic field was applied without charge current.

In contrast to TI layer, magnetic elements of soft magnet $Co_{40}Fe_{40}B_{20}$ layer have different responses with this external magnetic field in Fig.4.4. As shown in Fig.4.4 (a), there is a contrast of the magnitude of reflectivity with left and right circularly polarized light at Fe L_2 ($2p_{1/2}$) and L_3 ($2p_{3/2}$) edges, as a result of spin orientation due to the magnetization, which is also referred to as magnetic circular dichroism. Additionally, in Fig.4.4 (b), there is an obvious reflectivity dichroism with respect to left and right polarization RXR measurements, and the strength of this distinction has be emphasized at several specific incident angles, such as $\theta = 15°, 20°, 28°$. Therefore, $Co_{40}Fe_{40}B_{20}$ layer was fully magnetized by the magnetic field which is illustrated as the magnetic dichroism.

4.4 Discussion

Both RXR with tuning photon energy and varying reflectivity angle have been performed on multilayer thin film Al_2O_3 / $Co_{40}Fe_{40}B_{20}$ / $(Bi_{0.5}Sb_{0.5})_2Te_3$, with an in-plane magnetic field, and these measurement results are highly identical to what were expected. The feature of magnetization at magnetic elements, such as Fe L edges, can be easily probed by resonant reflectivity measurement. However, this magnetic field did not affect the equivalence of spin surface states in topological materials. To further study the spin polarization

and magnetization switch due to the spin-orbit torque (SOT), charge current has to be considered as a part of the experiment condition.

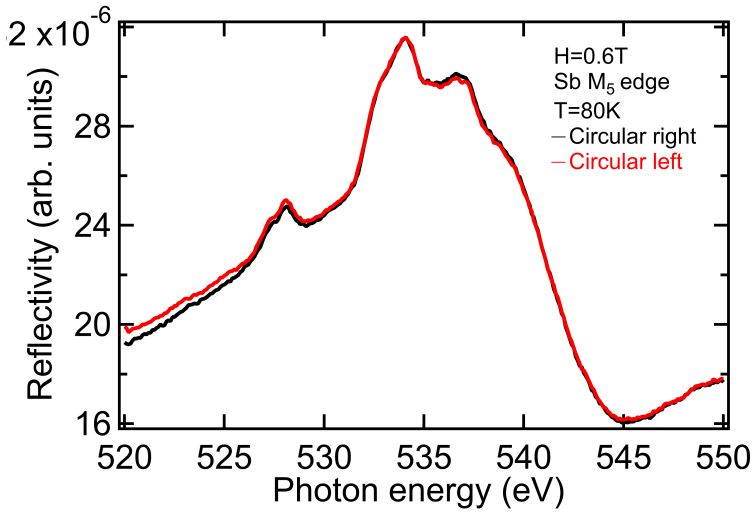

(a)

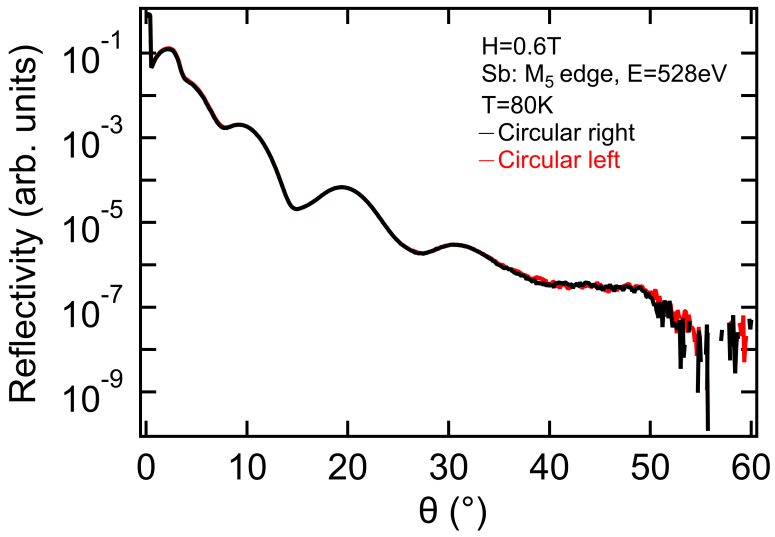

(b)

Figure 4.3: Resonant X-ray reflectivity (RXR) spectra of Al_2O_3/ $Co_{40}Fe_{40}B_{20}$/ $(Bi_{0.5}Sb_{0.5})_2Te_3$ multilayer thin film sample at Sb M_5 edge (a) Normalized RXR spectra of Al_2O_3/ $Co_{40}Fe_{40}B_{20}$/ $(Bi_{0.5}Sb_{0.5})_2Te_3$ at Sb M_5 edge in a magnetic field of 0.6T measured by circularly polarized soft X-ray at 80K. (b) RXR oscillation with angle dependence at Sb M_5 edge

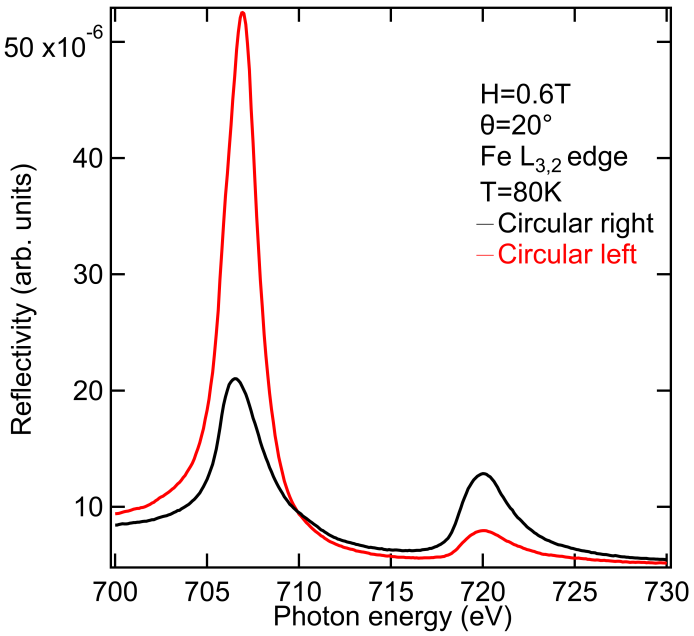

(a)

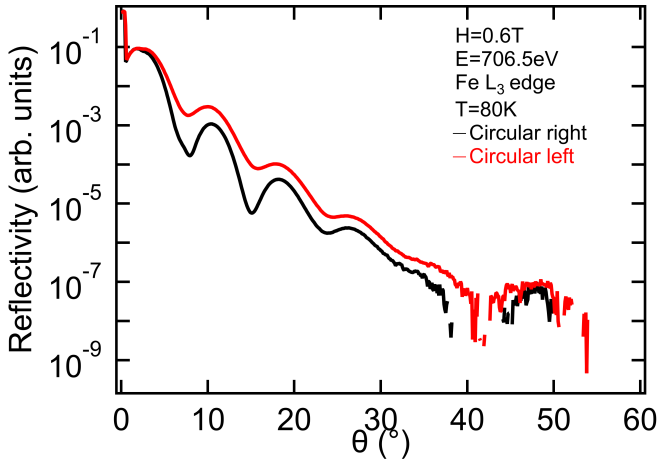

(b)

Figure 4.4: Resonant X-ray reflectivity (RXR) spectra of Al_2O_3 / $Co_{40}Fe_{40}B_{20}$ / $(Bi_{0.5}Sb_{0.5})_2Te_3$ multilayer thin film sample at Fe $L_{2,3}$ edges (a) Magnetic dichrosm illustrated in RXR of Al_2O_3 / $Co_{40}Fe_{40}B_{20}$ / $(Bi_{0.5}Sb_{0.5})_2Te_3$ at Fe $L_{2,3}$ edges in a magnetic field of 0.6T measured by circularly polarized soft X-ray at 80K. (b) RXR oscillation with angle dependence at Fe L_3 edge.

Chapter 5

Reflectivity Measurement with Charge Current of Multilayer Thin Film: Al_2O_3 / $Co_{40}Fe_{40}B_{20}$ / $(Bi_{0.5}Sb_{0.5})_2Te_3$

5.1 Overview

The spin polarization of topological insulator edge states can caused by a charge current passing through its surface due to the spin-momentum locking [33, 47], and the direction of spin current is perpendicular with the current direction (see in Fig.1.1). Because of the strong spin orbit interaction, this net spin current could influence and couple with magnetic angular momentum in the vicinity of TI/magnet interface, referred to as spin-orbit torque (SOT). As a result, the manipulation of magnetization is achieved by the charge current. From chapter 4, the resonant X-ray reflectivity (RXR) is able to probe magnetization with the dichroism effect. Similar idea was used to probe the magnetization at $Co_{40}Fe_{40}B_{20}$ layer attributed to spin orbit torque with RXR measurement, but the magnetic field was replaced by an in-plane current. By adjusting the current, we were expecting to observe the magnetic dichroism at magnetic element edges. In section 5.2, I will represent the details about electrical design and experiment challenges. More results and experiment parameters will be discussed in section 5.3. Finally, to summarize the experiments, there are several discussions whether these experiments were reasonable in section 5.4 based on the practical and theoretical aspects.

5.2 Reflectivity measurements

The reflectivity was measured with varying in-plane DC current at both room temperature (299K) and low temperature (23K). The sample has been mounted and wired on an electrical wiring sample plate, shown in Fig.5.1. When the sample plate is inserted and installed in the diffractometer, one end of the circuit directly connect the ground through the cryogenic frame, and the other end will contact with an external current source outside of UHV chamber through a feedthrough shown in Fig.3.6. However, since the wiring sample holder cannot be transferred through the loadlock, it always requires manually transferring the sample through the window by venting chamber. Because the UHV working pressure level is at 10^{-9} Torr, the chamber pumping down process needs three days to complete, leading to a huge time sacrifice and inefficiency.

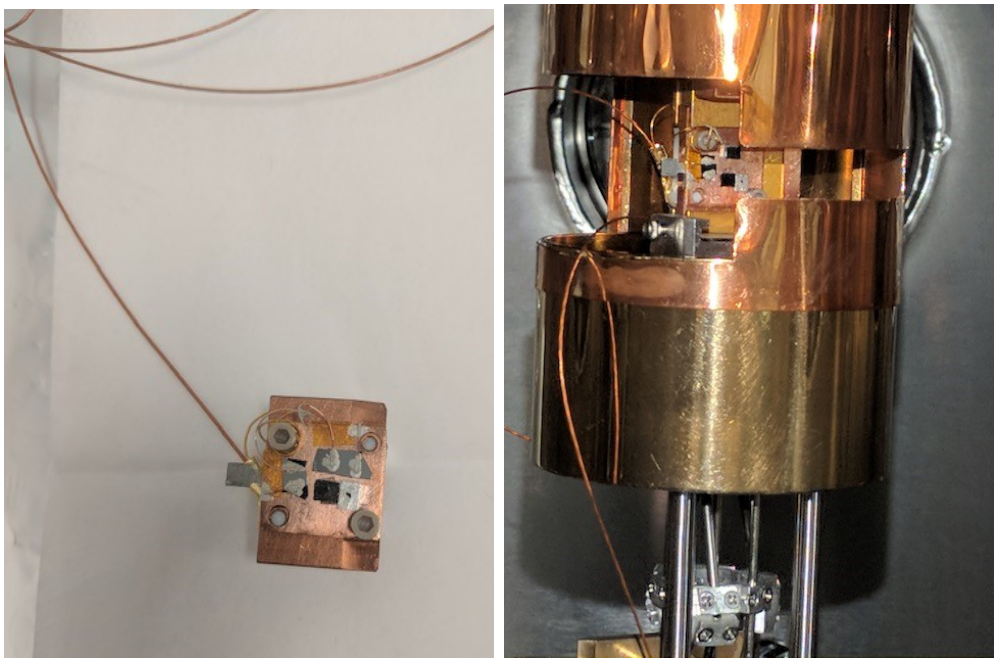

(a) (b)

Figure 5.1: Practical wiring in CLS' REIXS station. (a) Sample plate with a wiring electrode; (b) Installation of wired sample.

Fig.5.2 shows the circuit connection scheme of a DC current source with a voltage limit of 200V. Based on this scheme, a series of RXR measurements with various electric bias values ranging from 0 to ± 200 volts were operated on Al_2O_3 / $Co_{40}Fe_{40}B_{20}$

/ $(Bi_{0.5}Sb_{0.5})_2Te_3$ thin film, to induce the spin polarization at surface states. Besides, there were several efforts made to improve the device electronic properties and reduce the artificial errors.

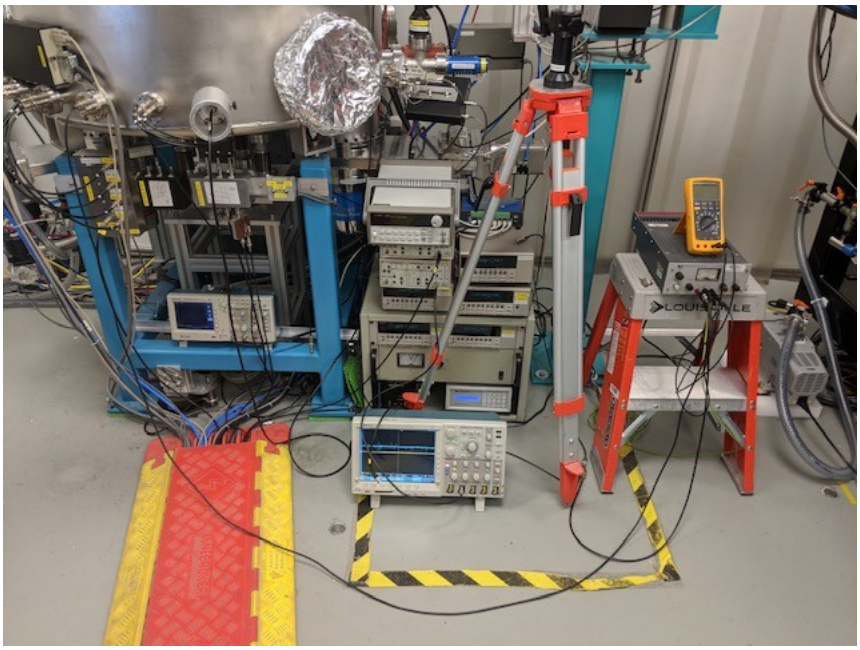

Figure 5.2: Electrical connection scheme between current source and sample

5.3 Results

5.3.1 RXR measurement

During the experiment, RXR was measured at both TI and magnetic element edges. Instead of detecting the magnetic dichroism by switching the polarization light, it was supposed to be observed by changing the bias polarities with a fixed polarized light. However, the refletivities at Co $L_{2,3}$ edges with opposite current directions has the sample lineshape, so there was no switch of magnetization at TI/magnetic interface induced with either continuous (Fig.5.3 (a)) or pulsed current (Fig.5.3 (b)). In addition, the cross section area (see in Fig.3.3) of the sample is $1.95 \times 10^{-7} cm^2$ with a 3mm width and a 6.5nm thickness, and the resistance of the sample is $5.52K\Omega$, so the current density can be calculated.

From Fig.5.3 (b), the maximum voltage performed was 75V, and the corresponding current density was $6.96 \times 10^4 \mathrm{A{\cdot}cm^{-2}}$. This current density is much smaller than what has been reported of the literature ($6 \times 10^5 \mathrm{A{\cdot}cm^{-2}}$)[44]. Therefore, one of the likely reasons of no observed dichroism is that insufficient spin polarization was induced by the current to manipulate the magnetization.

In Fig.5.3 (c) and (d), reflectivities was also measured at high (299K) and low temperatures (23K) with an applied current, in order to check if there was a temperature dependence of the spin polarization. What has been presented in these figures does not give the positive result, but the resistance of the thin film increased to $30K\Omega$ at 23K, which is around 10 times larger than the resistance at 299K. Since the sample was simply connected in circuit with silver paste shown in Fig.3.3 (b), it was easier to damage the connection with relatively large thermal expansions. Hence, this unexpected resistance change has been attributed to the unreliable electrical connection, which will be discussed later.

5.3.2 I-V characterization and sample device modification

There are two common ways to increase the current density. One of them is to increase the applied current, requiring a higher current limit electronic device, and the other one is to reduce the cross section without changing the current source. To effectively increase the current density, the later solution was performed. A new device was designed to reduced the cross section. As mentioned in section 3, by using lithography and ion milling techniques, a more confined and clean device with multiple widths was fabricated (see in Fig.3.4). With this new device, the current density can easily approach $10^5 \mathrm{A{\cdot}cm^{-2}}$ at the 50 μm thin part when we applied 20V as a source of current.

Moreover, the electronic connection was another significant factor influencing the results of measurement. Originally, the sample was wired with cleaved electrodes. This method not only introduced small dust particle contamination on the surface, it was also difficult to control the cleave depth. By contrast, a pair of 50nm thick Au electrodes were deposited on the ends of sample pattern with MBE technique on the new device. Additionally, if the sample directly connected with the wire installed on sample holder, it was easy to cause the destruction when the sample position had been modified with moving diffractometer motors. To eliminate this shortage, a stress relief device was added on the sample holder with silver epoxy, which introduced a medium metallic pad connecting the wire and sample electrode separately. (see in Fig.5.4)

The electric conductivity feature was improved incredibly by using both the Au elec-

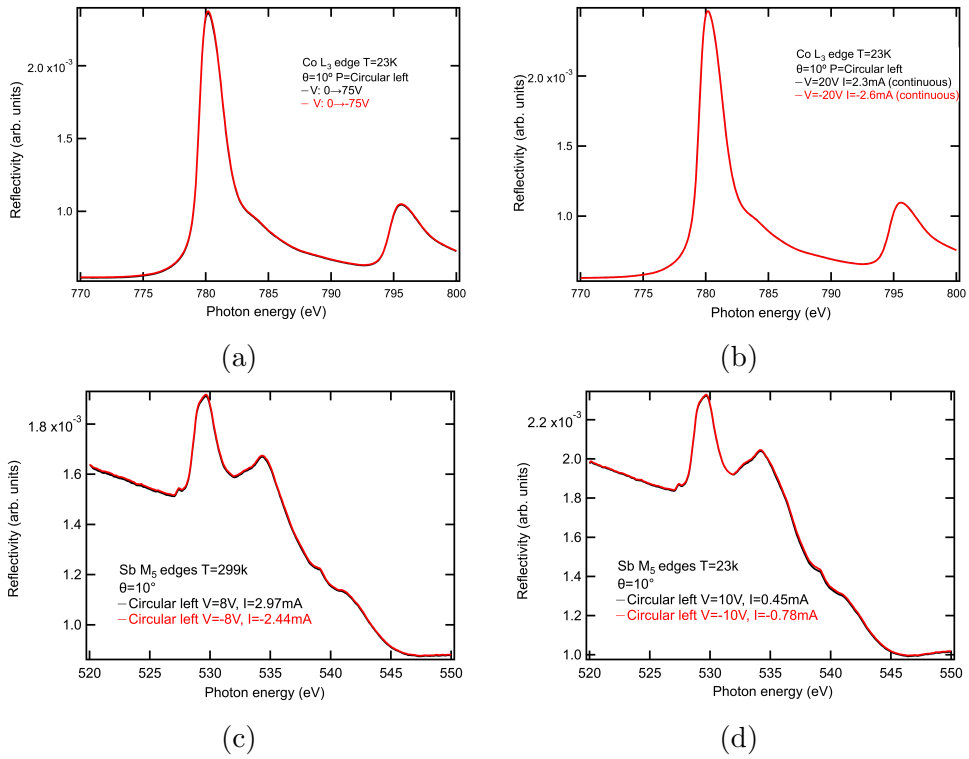

Figure 5.3: Resonant X-ray reflectivity (RXR) spectra of Al_2O_3 / $Co_{40}Fe_{40}B_{20}$ / $(Bi_{0.5}Sb_{0.5})_2Te_3$ multilayer thin film sample with DC current bias at Co L (a, b) and Sb M edges (c, d).

trode and stress relief device, which can be observed from the current-voltage (I-V) characterization. Fig.5.5 (a) and (b) illustrate the transport measurement of original bar shape and the fabricated device respectively. There was an obvious nonlinear response in Fig.5.5 (a) caused by the unstable connection. In contrast to the former case, the new device presented a stable resistance in both trivial environment and low temperature UHV system, and the resistance was stable at 12.3kΩ. (see in Fig.5.5 (b))

5.3.3 Beam size improvement

Although the fabricated new device solved the problem in terms of electrical connection and current density, another difficulty related beam position shift with relatively small sample area was created, which can be observed in Fig.5.6 (a). As mentioned in section 2,

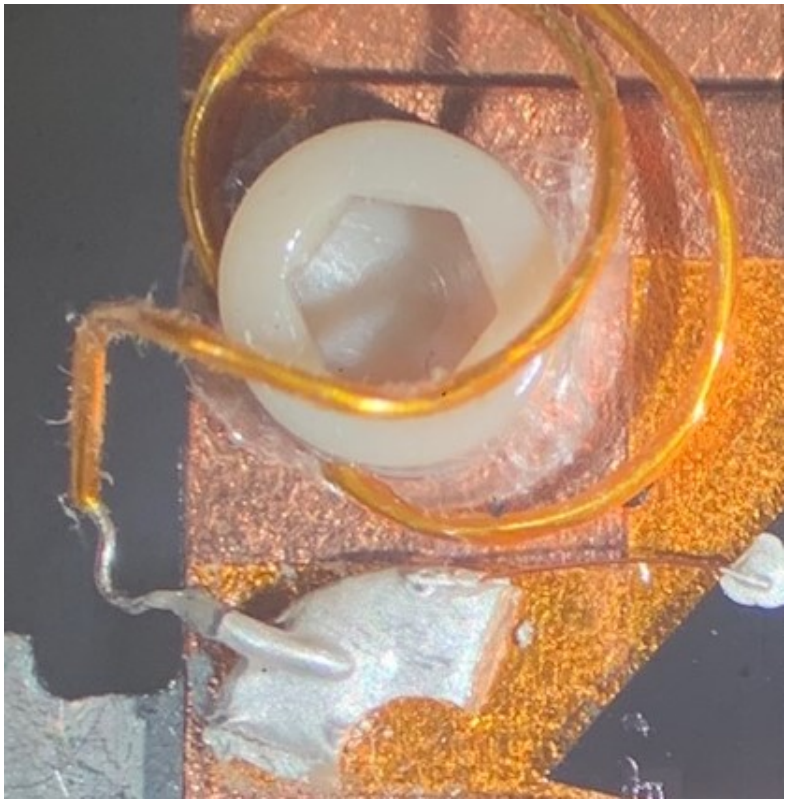

Figure 5.4: Stress release pad connecting the sample plate and the sample electrode.

the beam has a dimension of 150 $\times$ 300 μm^2, which is comparable with the sample width. As a result of photon polarization switch, the error of relative position changes of the beam spot increased, illustrated by a clear intensity split at off resonance energies in Fig.5.6 (a). To reduce this effect, we regulate the beam flux by reducing the optical component size from 4 to 1.6 mm. Fig.5.6 (b) shows an obvious improvement of beam shifting indicated by the overlap of left and right circular polarization results at the off resonance part.

5.3.4 Current conflict

With the new device fabricated the "L" shape pattern, the current density at 50μm width part achieved to $1.6 \times 10^5 \mathrm{A{\cdot}cm^{-2}}$ when the bias was 20V. There was no dichroism shown in reflectivity with respect to opposite bias polarities, see in Fig.5.7. As the bias increased to 200V, the Joule heat generated at thin part burned the device and formed an open circuit.

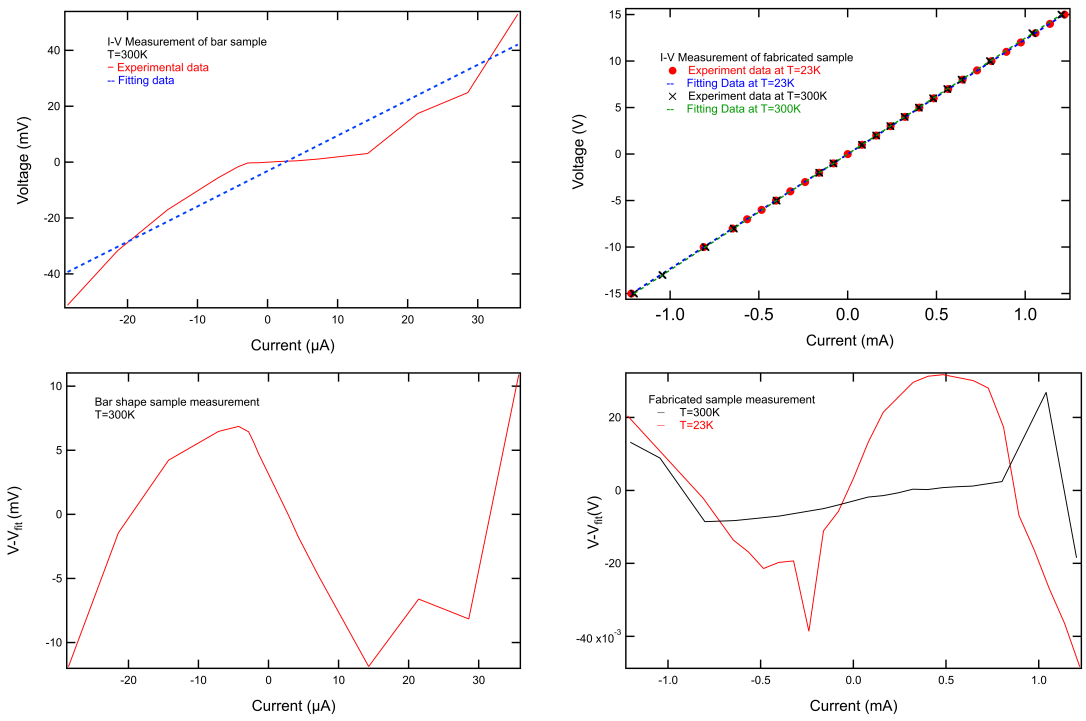

(a) (b)

Figure 5.5: Current-Voltage characterizations of thin film Al_2O_3 / $Co_{40}Fe_{40}B_{20}$ / $(Bi_{0.5}Sb_{0.5})_2Te_3$: (a) the I-V plot and voltage residual shows the nonlinear noisy response of the bar shape sample at room temperature; (b) the I-V plot and voltage residual shows the linear response of the fabricated shape sample at both room and low temperatures.

Therefore, there should be an upper limit of the total current density in order to avoid generating too much heat to damage the circuit. Fig.5.8 shows the TEY signal went to zero as z=0.2 corresponding to the junction between 50μm and 2mm width area. However, since both the TI and magnet layers conduct current, the current passing through the TI layers will be less than the total current applied to the whole device. Consequently, it reduces the total spin current for a given current source. This shunting effect may become dominant when the resistivity of the magnet is much smaller than TI, or the distribution of the thickness is not appropriate [45].

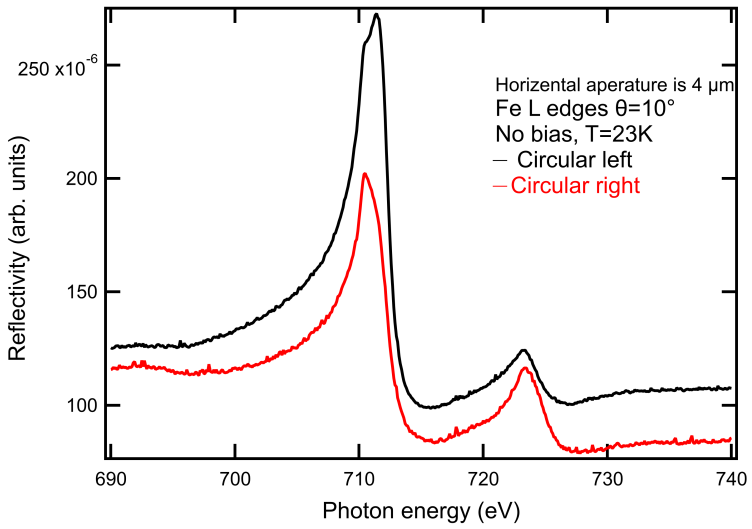

(a)

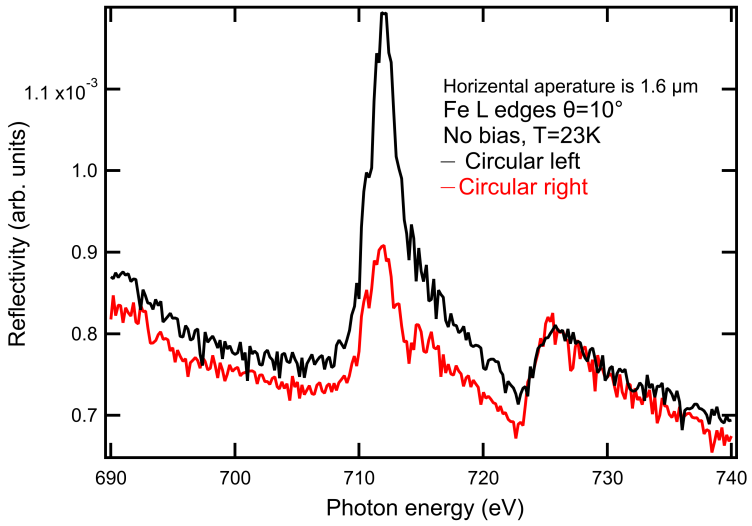

(b)

Figure 5.6: Beam size influence of fabricated device. (a) RXR measurements with normal beam aperture at Fe L edges; (b) RXR measurements with reduced beam aperture (1.6mm) at Fe L edges with a sacrifice of half signals.

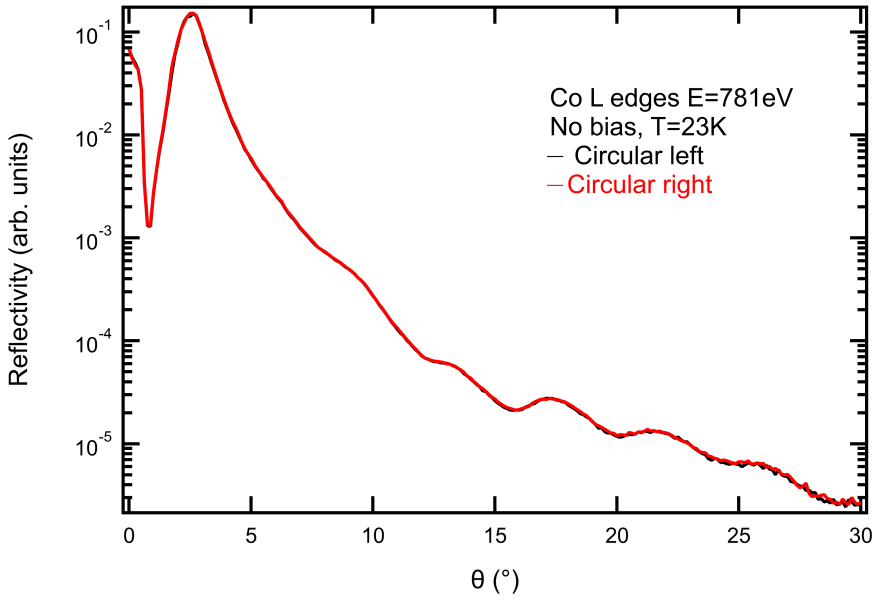

Figure 5.7: Resonant X-ray reflectivity (RXR) spectra as a function of incident angle at Co L_3 edge with 20V DC bias.

5.4 Discussion

Current density is one of the most important parameters dominating the magnetic environment of TI/magnet bilayer thin film. With nanofabrication techniques, the sample has been nicely defined in smaller widths, and the electronic connection was more stable. By reducing the cross section, the maximum current density has achieved $10^5 \mathrm{A{\cdot}cm^{-2}}$ with a 20V DC bias. However, the Joule heat generated at the 100μm junction broke the electrical circuit when the voltage was 200V. Additionally, the shunting effect could reduce the practical current density applied to the topological layer, which caused a conflict between the upper current limit and the insufficient current density of spin current.

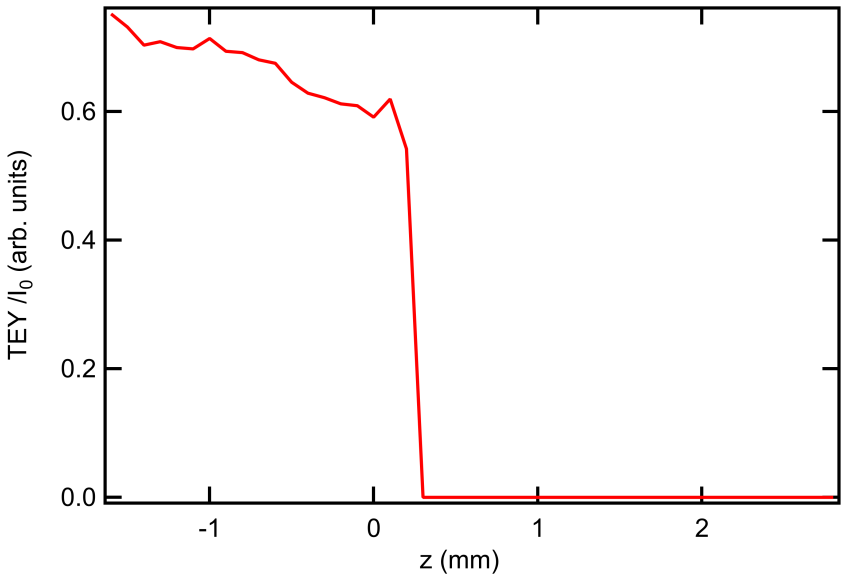

Figure 5.8: Total Electron Yield (TEY) signal measured in z direction with 200V bias.

Chapter 6

New Material Measurement: $MgO/$ $Cr_{0.9}(Bi_{0.5}Sb_{0.5})_{1.9}Te_3/$ $(Bi_{0.5}Sb_{0.5})_2Te_3$

6.1 Overview

Electric field manipulation of magnetic order has proven itself to be of both fundamental and technological importance in spintronic devices [32, 2, 46, 30]. In the previous Chapters, we have studied and discussed the current induced spin polarization of the TI and magnet bilayer structure. There is a new material candidate, Cr-doped TI thin film, which is also able to gain the magnetization induced by spin orbit torque, reported in the literature [29, 11, 10]. The effective electric-field control of spin orbit torque and the giant spin-torque efficiency in Cr-doped TI may lead to the development of energy-efficient spintronic devices [10]. In this chapter, a brand new sample with $MgO/$ $Cr_{0.9}(Bi_{0.5}Sb_{0.5})_{1.9}Te_3/(Bi_{0.5}Sb_{0.5})_2Te_3$ will be studied with RXR method at Cr L edge. Unlike the bilayer device, this insulate magnet does not require a saturation effective magnetic field to trigger the magnetization transformation. Several features of this new magnetic topological material with a new electronic device will be presented and discussed.

6.2 Reflectivity measurements

The $MgO/$ $Cr_{0.9}(Bi_{0.5}Sb_{0.5})_{1.9}Te_3/(Bi_{0.5}Sb_{0.5})_2Te_3$ thin film grown on a sapphire substrate has been fabricated in the same shape mentioned in section 5, which can be seen in Fig.3.4, and similar RXR measurement was done at Cr L_3 edge without current.

In contrast to previous experiments, the DC voltage source was replace by a lock-in amplifier, which can generate an AC signal with 0 to 5V amplitude and 0 to 1000Hz frequency. This Signal Recovery 7625 DSP lock-in amplifier can isolate current/voltage signals oscillating at a reference frequency amongst a large noise background of other frequencies. In our experiment, the sample voltage/current was driven by the lock-in amplifier and used as the reference frequency. Oscillations of the photodiode current at this same frequency were measured which should correspond to a direct measure of current induced dichrosm. Because of the measurement of the lock-in signal, the noise level of the circuit environment can be monitored, and the phase difference between reference and input signal is able to be observed.

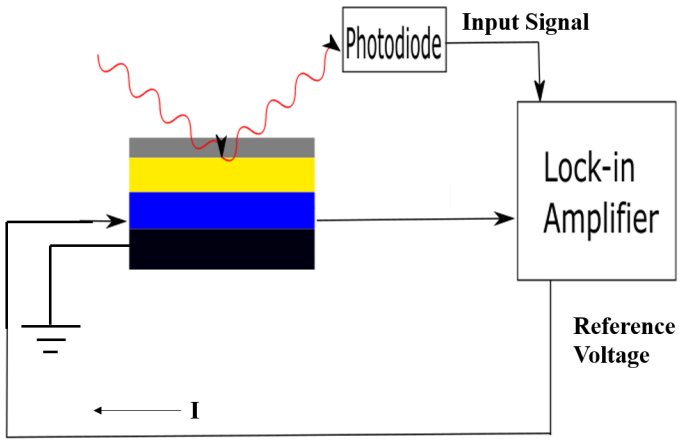

Figure 6.1: Scheme of reflectivity measurement through the lock-in amplifier.

In addition, the new material's electronic transport properties was checked by an in-situ I-V measurement at 3.9K and 10^{-9} Torr vacuum level, and the bias has been applied on sample ranging from 0 to 200V.

6.3 Results

6.3.1 I-V measurement

Figure 6.2 here illustrates a nonlinear response of I-V measurement when the voltage was applied from 0 to 200V at low temperature (3.9K). According to this result, the resistance

of new film $MgO/\ Cr_{0.9}(Bi_{0.5}Sb_{0.5})_{1.9}Te_3/\ (Bi_{0.5}Sb_{0.5})_2Te_3$ is 403.32kΩ, which is much larger than the resistance of the Al_2O_3 / $Co_{40}Fe_{40}B_{20}$ / $(Bi_{0.5}Sb_{0.5})_2Te_3$ thin film. One of the possible reason is the damage caused in fabrication process. By checking the surface condition with the MA61A OLYMPUS microscope, some evidence can be found on the sample surface, as shown in Fig.6.3. In Fig.6.3 (a) to (c), the resistance of samples are 150, 155, and 158 KΩ respectively, which is increasing with the increased amount of scratch. As a result, the resistance is directly related to the sample surface quality. Another likely reason causing this large resistance is my inappropriate operation during the fabrication. In the sample preparation process, the ultrasonic bath heat of Remover PG solution (a strong base) was used to get rid of the photoresist. However, since the $Cr_{0.9}(Bi_{0.5}Sb_{0.5})_{1.9}Te_3$ was grown by MBE technique, the large amplitude horizontal oscillation of the ultrasonic cleanser is able to damage the layer structure of the sample, which may lead to a destruction of the topology for this Cr doped TI.

6.3.2 Reflectivity measurement with lock-in amplifier

The maximum Cr L_3 absorption edge was checked by the reflectivity measurement verses photon energy. From Fig.6.4 (a), the reflectivity with respect to varying photon energy has a peak at 576.8eV when the incident angle is 7.5°. In Fig.6.4 (b), resonant X-ray reflectivity of the $MgO/\ Cr_{0.9}(Bi_{0.5}Sb_{0.5})_{1.9}Te_3/\ (Bi_{0.5}Sb_{0.5})_2Te_3$ film as a function of angle with the photon energy at Cr L_3 absorption edge at 23K determined no dichroism without current, and the fringes at specific angles represented the constructive interference of the atomic interfaces.

Since the photodiode was connected with the amplifier as a input source modulated with a referenced voltage signal generated by the amplifier, the reflectivity signal was monitored by the phase difference between the AC input signal and reflected photons. When the photon energy was adjusted to 576.8eV (Cr L_3 edge), the phase difference was checked while the circular polarization type switched from left to right at several individual incident angles: $\theta = 7.5°, 12.5°, 16.5°, 20.5°, 28°$. However, there was no reliable phase change captured. In addition, at the incident angle, when the detector was adjusted to off position in a few degree angle, no significant modification of the phase has been observed. When the current density was 0.15 A·cm^{-2}, the noise level at 10 to 100fA was recorded with a 50s of timeconstant during the measurement. Correspondingly, the signal to noise ratio is around 0.01%. This noisy background will be studied and eliminated in the future. So far, there is no effective reflectivity results determining the clear spin-orbit torque at Cr L edge under the AC condition.

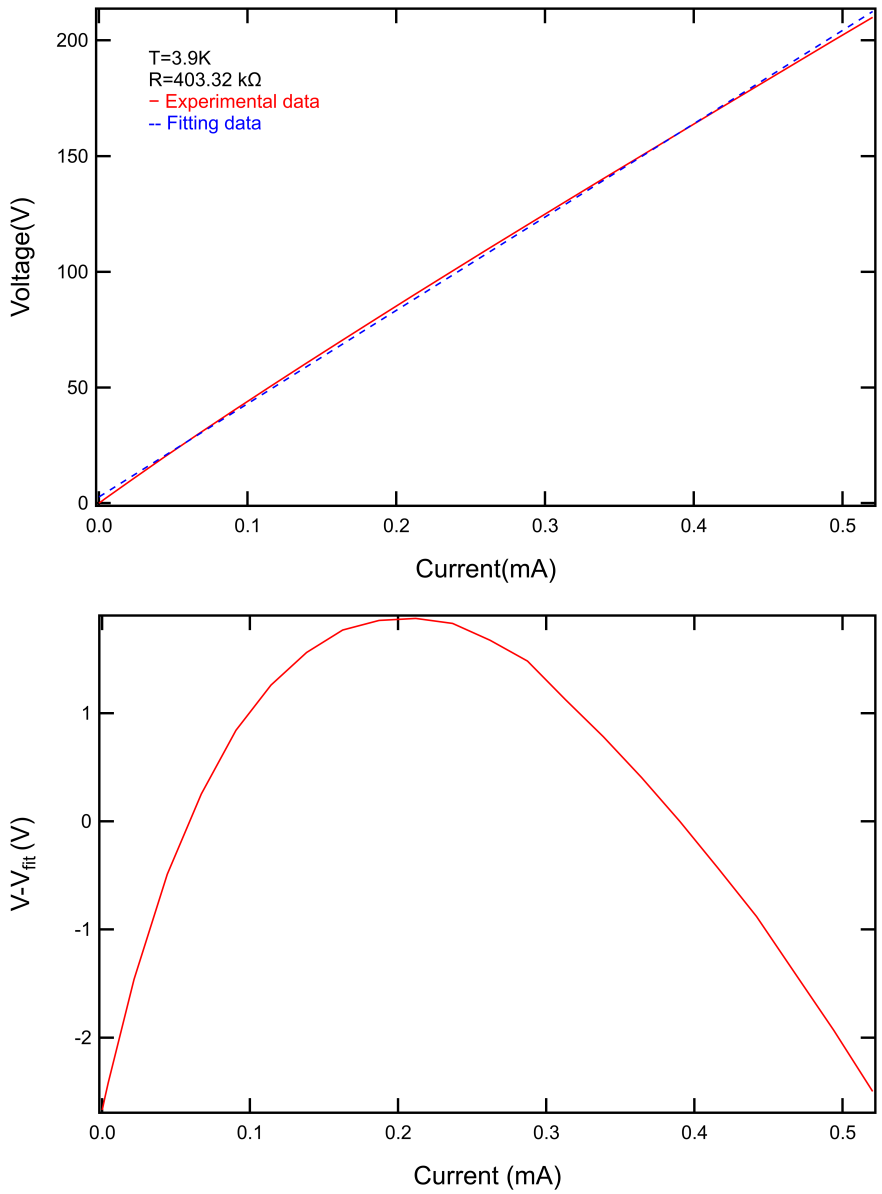

Figure 6.2: Conductive transport measurement of $MgO/\ Cr_{0.9}(Bi_{0.5}Sb_{0.5})_{1.9}Te_3/\ (Bi_{0.5}Sb_{0.5})_2Te_3$ topological magnet thin film.

In addition, the lowest temperature that can be approached at CLS was 23K, which is higher than the critical temperature of Cr (T_C=13K), so it was hard to generate the ferro-

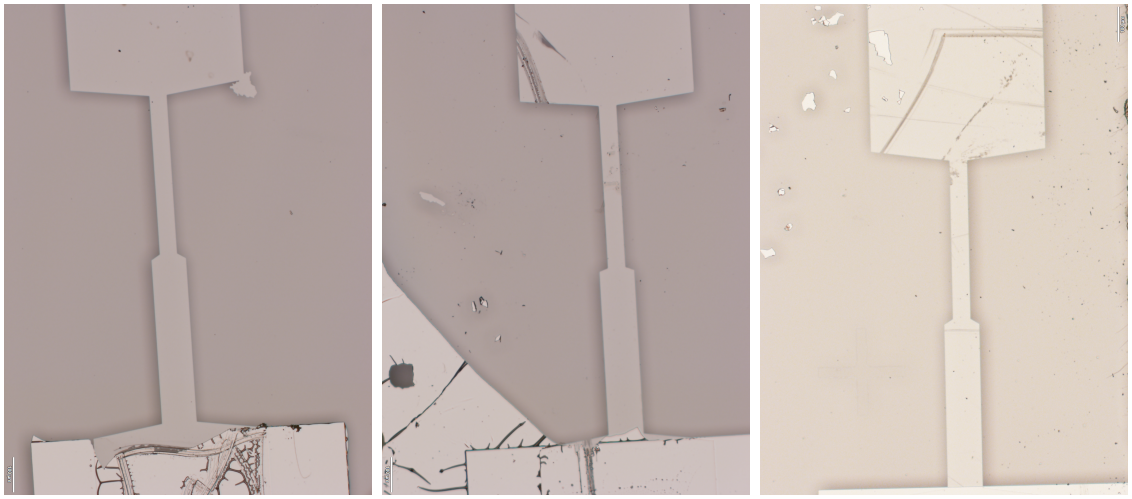

(a) (b) (c)

Figure 6.3: Surface situation of thin film $MgO/\ Cr_{0.9}(Bi_{0.5}Sb_{0.5})_{1.9}Te_3/\ (Bi_{0.5}Sb_{0.5})_2Te_3$ by microscope. Samples with resistance: (a) R=150KΩ;(b) R=155KΩ; (c) R=158KΩ, respectively

magnetic order at this Cr doped thin film. Therefore, the magnetization due to the charge current could be influenced by this temperature limit, and the reflectivity measurement should be further studied under the lower temperature condition.

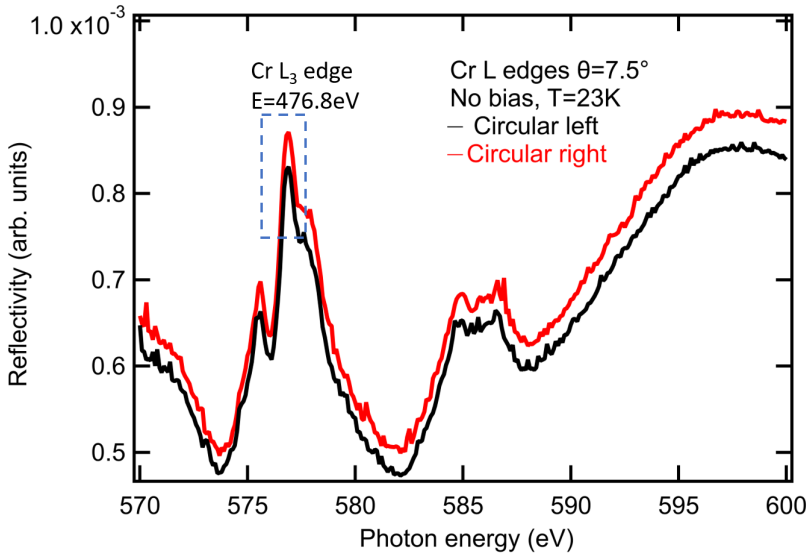

(a)

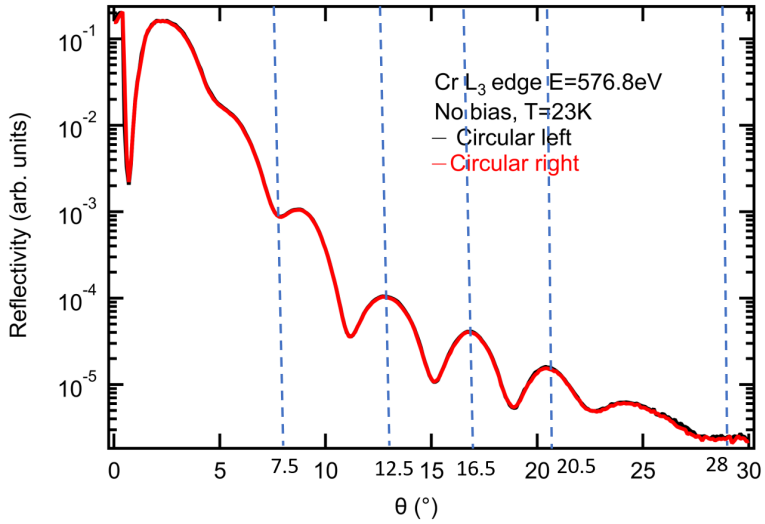

(b)

Figure 6.4: Resonant X-ray reflectivity at Cr L_3 edge of $MgO/\ Cr_{0.9}(Bi_{0.5}Sb_{0.5})_{1.9}Te_3/\ (Bi_{0.5}Sb_{0.5})_2Te_3$ thin film without bias at 23K.(a) Reflectivity at $\theta = 7.5°$ as a function of photon energy with left and right circularly polarized light; (b) Reflectivity verses angle of incidence measured at the peak of the Cr L_3 edge.

Chapter 7

Conclusions and Future Work

7.1 Summary of results

An overarching motivation of this thesis has been to study the nature of spin polarization of topological material surface states with performing the resonant X-ray reflectometry (RXR). Some efforts, in both measurement technique and sample quality, have been done in the experiment process to improve the spin polarization detection progressively. Although there is no positive conclusions that can be drawn from the experiments, it is important to reflect upon and discuss these results in order to guide the subsequent project.

For TI/magnet bilayer and thin film, one of the most important experiment conditions is the current density which has been discussed a lot in this thesis. Several efforts have been made to maintain a sufficient and stable charge current. In chapter 5, the charge current has been successfully increasing to $10^5 \mathrm{A{\cdot}cm^{-2}}$ by fabricating the thin film to an expected small width shape. Also, with performing the fabrication techniques, Au electrodes deposited at the sample ends significantly reduce the wiring difficulty and the contamination at the sample surface. As has been shown in the I-V characterizations, the risk of silver past connection destruction is effectively eliminated by the add on stress relief pad. With regards to the reflectivity measurement technique, the basis of the advanced synchrotron light source has been studied and explored, such as the beanline scheme, diffractometer structure, and adjustment of the beam size.

On the other hand, there are still some obstacles to overcome. There is still a request to figure out the critical current density corresponding to the Al_2O_3 / $Co_{40}Fe_{40}B_{20}$ / $(Bi_{0.5}Sb_{0.5})_2Te_3$ thin film. In addition,the shunting effect may influence the current density

of the topological insulator layer since the resistivity of the magnet is much smaller than TI, or the distribution of the thickness is not reasonable [45]. Moreover, when a DC current is applied as the current source, the current density cannot be too high which may cause the burning of sample leading to an open circuit. According to this, a conflict in current density is generated. Finally, the low efficiency of loading sample is also a big obstacle to overcome.

Regarding to the new Cr doped topological magnet thin film, there are some attempts which has been made on this new sample. The electronic device, called lock-in amplifier, was applied as a current source. With this device, the noise level, which was 0.01% was first measured and studied, which can guide a further improvement in the electrical design. Besides, the electronic property of this topological magnet thin film has been studied with a transport measurement at extreme low temperature (3.9K), which can be regarded as a reference for the future study.

However, there are some doubts for $MgO/\ Cr_{0.9}(Bi_{0.5}Sb_{0.5})_{1.9}Te_3/\ (Bi_{0.5}Sb_{0.5})_2Te_3$ thin film. One of them is the high resistance ($100K\Omega$). In contrast to the similar material reported in other experiments [11, 4], the resistance of thin kind of material is supposed to be around 10KΩ. Besides, the critical temperature (T_C) of Cr is 13K, but the lowest temperature achieved is 23K in our the experiment at REIXS, and it is possible that the dichroism at Cr edge due to the spin-orbit torque could be enhanced by the ferromagnetic feature.

7.2 Future work

A few projects come to mind when considering what else could be done to study the RXR and answer the questions regarding to the nature of spin polarization and SOT of TIs.

Firstly, a scheme for analyzing resonant soft x-ray reflectivity data should be developed, which takes the atomic structure of a material into account by "slicing" it into atomic planes with characteristic optical properties. Although we have collected a lot of RXR data with the multilayer thin film, they have not been studied quantitatively by a theoretical model which allows for a reliable extraction of spectral information about a specific layer of atoms between the interfaces. It also enables to calculate the spin polarization or spin-orbit torque efficiency based on the sample structure with a certain value of current, so that there will be a quantitative expectation for the current density used to manipulate the magnetization.

There is also an opportunity to solve the current density requirement. Due to the conflict between the high current density request and upper limit to avoid causing damage

on sample device, it worthwhile to figure out a new way to supply the current. A potential device is a waveform generator, which allows to provide a current in a form of short time pules, such as 100ns. In addition, this kind of device is able to give more possibility of measurement waveform of current signal, so that we have more opportunities to choose a satisfied current form.

Finally, to solve the low efficiency of the sample loading, a new in-situ wiring device is expected to be designed and applied to the elastic scattering system in CLS. This new device will install a two-channel plastic part on the sample receptacle serving as permanent electrodes, and two spring load POGO pins will be added on the backside of the sample plate in order to connect the sample into electrical circuit. More details of the design will be provided in Appendix A. This in-situ wiring device allows to achieve sample loading in 40 min without breaking the vacuum environment. In contrast with the previous method of wiring sample loading mentioned in section 5, this in-situ wiring system not only reduces the loading time leading to a high efficiency RXR measurement, but also promises the stability of measurement environment.

References

[1] Jens Als-Nielsen, Des McMorrow, and Ian Robinson. Elements of modern x-ray physics. *Physics Today*, 55(3):64–66, 2002.

[2] Can Onur Avci, Andy Quindeau, Chi-Feng Pai, Maxwell Mann, Lucas Caretta, Astera S Tang, Mehmet C Onbasli, Caroline A Ross, and Geoffrey SD Beach. Current-induced switching in a magnetic insulator. *Nature materials*, 16(3):309, 2017.

[3] Donald H Bilderback, Pascal Elleaume, and Edgar Weckert. Review of third and next generation synchrotron light sources. *Journal of Physics B: Atomic, molecular and optical physics*, 38(9):S773, 2005.

[4] Cui-Zu Chang, Jinsong Zhang, Xiao Feng, Jie Shen, Zuocheng Zhang, Minghua Guo, Kang Li, Yunbo Ou, Pang Wei, Li-Li Wang, et al. Experimental observation of the quantum anomalous hall effect in a magnetic topological insulator. *Science*, 340(6129):167–170, 2013.

[5] CT Chen, YU Idzerda, H-J Lin, NV Smith, G Meigs, E Chaban, GH Ho, E Pellegrin, and F Sette. Experimental confirmation of the x-ray magnetic circular dichroism sum rules for iron and cobalt. *Physical review letters*, 75(1):152, 1995.

[6] CT Chen, F Sette, Y Ma, and Silvio Modesti. Soft-x-ray magnetic circular dichroism at the $L_{2,3}$ edges of nickel. *Physical Review B*, 42(11):7262, 1990.

[7] André Dankert, Johannes Geurs, M Venkata Kamalakar, Sophie Charpentier, and Saroj P Dash. Room temperature electrical detection of spin polarized currents in topological insulators. *Nano letters*, 15(12):7976–7981, 2015.

[8] Sergio Di Matteo. Resonant x-ray diffraction: multipole interpretation. *Journal of Physics D: Applied Physics*, 45(16):163001, 2012.

[9] H Ebert, J Stöhr, SSP Parkin, M Samant, and A Nilsson. L-edge x-ray absorption in fcc and bcc Cu metal: Comparison of experimental and first-principles theoretical results. *Physical Review B*, 53(23):16067, 1996.

[10] Yabin Fan, Xufeng Kou, Pramey Upadhyaya, Qiming Shao, Lei Pan, Murong Lang, Xiaoyu Che, Jianshi Tang, Mohammad Montazeri, Koichi Murata, et al. Electric field control of spin-orbit torque in a magnetically doped topological insulator. *Nature nanotechnology*, 11(4):352, 2016.

[11] Yabin Fan, Pramey Upadhyaya, Xufeng Kou, Murong Lang, So Takei, Zhenxing Wang, Jianshi Tang, Liang He, Li-Te Chang, Mohammad Montazeri, et al. Magnetization switching through giant spin-orbit torque in a magnetically doped topological insulator heterostructure. *Nature materials*, 13(7):699, 2014.

[12] Liang Fu and C. L. Kane. Time reversal polarization and a Z_2 adiabatic spin pump. *Phys. Rev. B*, 74:195312, Nov 2006.

[13] Liang Fu and C. L. Kane. Superconducting proximity effect and majorana fermions at the surface of a topological insulator. *Phys. Rev. Lett.*, 100:096407, Mar 2008.

[14] Pietro Gambardella and Ioan Mihai Miron. Current-induced spin-orbit torques. *Philosophical Transactions of the Royal Society A: Mathematical, Physical and Engineering Sciences*, 369(1948):3175–3197, 2011.

[15] Xingyu Gao, Swee Ching Tan, ATS Wee, Junhua Wu, Lingbing Kong, Xiaojiang Yu, and HO Moser. Structural and magnetic characterization of soft-magnetic feco alloy nanoparticles. *Journal of electron spectroscopy and related phenomena*, 150(1):11–14, 2006.

[16] Sanjeev Gautam, Shanshank N Kane, B-G Park, J-Y Kim, LK Varga, J-H Song, and Keun Hwa Chae. XAS and XMCD studies of amorphous FeCo-based ribbons. *Journal of Non-Crystalline Solids*, 357(11-13):2228–2231, 2011.

[17] Jiahao Han, Anthony Richardella, Saima A Siddiqui, Joseph Finley, Nitin Samarth, and Luqiao Liu. Room-temperature spin-orbit torque switching induced by a topological insulator. *Physical review letters*, 119(7):077702, 2017.

[18] JP Hannon, GT Trammell, M Blume, and Doon Gibbs. Erratum: X-ray resonance exchange scattering. *Physical Review Letters*, 62:2644, 1989.

[19] M. Z. Hasan and C. L. Kane. Colloquium: Topological insulators. *Rev. Mod. Phys.*, 82:3045–3067, Nov 2010.

[20] DG Hawthorn, F He, L Venema, H Davis, AJ Achkar, J Zhang, R Sutarto, H Wadati, A Radi, T Wilson, et al. An in-vacuum diffractometer for resonant elastic soft x-ray scattering. *Review of Scientific Instruments*, 82(7):073104, 2011.

[21] DG Hawthorn, F He, L Venema, H Davis, AJ Achkar, J Zhang, R Sutarto, H Wadati, A Radi, T Wilson, et al. An in-vacuum diffractometer for resonant elastic soft x-ray scattering. *Review of Scientific Instruments*, 82(7):073104, 2011.

[22] J Henk, M Hoesch, J Osterwalder, A Ernst, and P Bruno. Spin–orbit coupling in the L-gap surface states of Au (111): spin-resolved photoemission experiments and first-principles calculations. *Journal of Physics: Condensed Matter*, 16(43):7581, 2004.

[23] Yew San Hor, A Richardella, Pedram Roushan, Yuqi Xia, Joseph G Checkelsky, Ali Yazdani, Md Zahid Hasan, Nai Phuan Ong, and Robert Joseph Cava. p-type Bi_2Se_3 for topological insulator and low-temperature thermoelectric applications. *Physical Review B*, 79(19):195208, 2009.

[24] David Hsieh, Dong Qian, Lewis Wray, YuQi Xia, Yew San Hor, Robert Joseph Cava, and M Zahid Hasan. A topological dirac insulator in a quantum spin hall phase. *Nature*, 452(7190):970, 2008.

[25] David Hsieh, Yuqi Xia, Dong Qian, L Wray, JH Dil, Fedorov Meier, J Osterwalder, L Patthey, JG Checkelsky, Nai Phuan Ong, et al. A tunable topological insulator in the spin helical dirac transport regime. *Nature*, 460(7259):1101, 2009.

[26] Ron Jenkins. *Quantitative X-ray spectrometry*. CRC Press, 1995.

[27] Manabu Kanou and Takao Sasagawa. Crystal growth and electronic properties of a 3d rashba material, BiTeI, with adjusted carrier concentrations. *Journal of Physics: Condensed Matter*, 25(13):135801, 2013.

[28] C. Klewe, T. Kuschel, J.-M. Schmalhorst, F. Bertram, O. Kuschel, J. Wollschläger, J. Strempfer, M. Meinert, and G. Reiss. Static magnetic proximity effect in $\mathrm{Pt/ni}_{1-x}\mathrm{fe}_x$ bilayers investigated by x-ray resonant magnetic reflectivity. *Phys. Rev. B*, 93:214440, Jun 2016.

[29] Xufeng Kou, Liang He, Murong Lang, Yabin Fan, Kin Wong, Ying Jiang, Tianxiao Nie, Wanjun Jiang, Pramey Upadhyaya, Zhikun Xing, et al. Manipulating surface-related ferromagnetism in modulation-doped topological insulators. *Nano letters*, 13(10):4587–4593, 2013.

[30] CH Li, OMJ Vant Erve, JT Robinson, Y Liu, L Li, and BT Jonker. Electrical detection of charge-current-induced spin polarization due to spin-momentum locking in Bi_2Se_3. *Nature nanotechnology*, 9(3):218, 2014.

[31] Luqiao Liu, O. J. Lee, T. J. Gudmundsen, D. C. Ralph, and R. A. Buhrman. Current-induced switching of perpendicularly magnetized magnetic layers using spin torque from the spin hall effect. *Phys. Rev. Lett.*, 109:096602, Aug 2012.

[32] Yang Liu, Jean Besbas, Yi Wang, Pan He, Mengji Chen, Dapeng Zhu, Yang Wu, Jong Min Lee, Lan Wang, Jisoo Moon, et al. Direct visualization of current-induced spin accumulation in topological insulators. *Nature communications*, 9(1):2492, 2018.

[33] Farzad Mahfouzi, Naoto Nagaosa, and Branislav K Nikolić. Spin-orbit coupling induced spin-transfer torque and current polarization in topological-insulator/ferromagnet vertical heterostructures. *Physical review letters*, 109(16):166602, 2012.

[34] Jorg Maser. Soft x-rays and extreme ultraviolet radiation: Principles and applications. *Microscopy and Microanalysis*, 7(6):536–536, 2001.

[35] AR Mellnik, JS Lee, A Richardella, JL Grab, PJ Mintun, Mark H Fischer, Abolhassan Vaezi, Aurelien Manchon, E-A Kim, Nitin Samarth, et al. Spin-transfer torque generated by a topological insulator. *Nature*, 511(7510):449, 2014.

[36] Ioan Mihai Miron, Kevin Garello, Gilles Gaudin, Pierre-Jean Zermatten, Marius V Costache, Stéphane Auffret, Sébastien Bandiera, Bernard Rodmacq, Alain Schuhl, and Pietro Gambardella. Perpendicular switching of a single ferromagnetic layer induced by in-plane current injection. *Nature*, 476(7359):189, 2011.

[37] Reiko Nakajima, J Stöhr, and Yves U Idzerda. Electron-yield saturation effects in l-edge x-ray magnetic circular dichroism spectra of Fe, Co, and Ni. *Physical Review B*, 59(9):6421, 1999.

[38] Xiao-Liang Qi and Shou-Cheng Zhang. The quantum spin hall effect and topological insulators. *arXiv preprint arXiv:1001.1602*, 2010.

[39] Dongsheng Song, Ziqiang Wang, and Jing Zhu. Magnetic measurement by electron magnetic circular dichroism in the transmission electron microscope. *Ultramicroscopy*, 201:1–17, 2019.

[40] Joachim Stöhr and Hans Christoph Siegmann. Magnetism. *Solid-State Sciences. Springer, Berlin, Heidelberg*, 5, 2006.

[41] Jifa Tian, Isaac Childres, Helin Cao, Tian Shen, Ireneusz Miotkowski, and Yong P Chen. Topological insulator based spin valve devices: Evidence for spin polarized transport of spin-momentum-locked topological surface states. *Solid State Communications*, 191:1–5, 2014.

[42] Gerrit van der Laan and Adriana I Figueroa. X-ray magnetic circular dichroisma versatile tool to study magnetism. *Coordination Chemistry Reviews*, 277:95–129, 2014.

[43] Yi Wang, Praveen Deorani, Karan Banerjee, Nikesh Koirala, Matthew Brahlek, Seongshik Oh, and Hyunsoo Yang. Topological surface states originated spin-orbit torques in Bi_2Se_3. *Physical review letters*, 114(25):257202, 2015.

[44] Yi Wang, Dapeng Zhu, Yang Wu, Yumeng Yang, Jiawei Yu, Rajagopalan Ramaswamy, Rahul Mishra, Shuyuan Shi, Mehrdad Elyasi, Kie-Leong Teo, et al. Room temperature magnetization switching in topological insulator-ferromagnet heterostructures by spin-orbit torques. *Nature communications*, 8(1):1364, 2017.

[45] W. J. Xu, B. Zhang, Z. Wang, S. S. Chu, W. Li, Z. B. Wu, R. H. Yu, and X. X. Zhang. Scaling law of anomalous hall effect in Fe/Cu bilayers. *The European Physical Journal B*, 65(2):233–237, Sep 2008.

[46] K Yasuda, A Tsukazaki, R Yoshimi, K Kondou, KS Takahashi, Y Otani, M Kawasaki, and Y Tokura. Current-nonlinear hall effect and spin-orbit torque magnetization switching in a magnetic topological insulator. *Physical review letters*, 119(13):137204, 2017.

[47] Oleg V Yazyev, Joel E Moore, and Steven G Louie. Spin polarization and transport of surface states in the topological insulators Bi_2Se_3 and Bi_2Te_3 from first principles. *Physical review letters*, 105(26):266806, 2010.

[48] Mao Ye, Wei Li, Siyuan Zhu, Yukiharu Takeda, Yuji Saitoh, Jiajia Wang, Hong Pan, Munisa Nurmamat, Kazuki Sumida, Fuhao Ji, et al. Carrier-mediated ferromagnetism in the magnetic topological insulator Cr-doped $(Sb, Bi)_2Te_3$. *Nature communications*, 6:8913, 2015.

[49] P Zaumseil. X-ray reflectivity characterisation of thin-film and multilayer structures. In *Materials for Information Technology*, pages 497–505. Springer, 2005.

[50] Haijun Zhang, Chao-Xing Liu, Xiao-Liang Qi, Xi Dai, Zhong Fang, and Shou-Cheng Zhang. Topological insulators in Bi_2Se_3, Bi_2Te_3 and Sb_2Te_3 with a single dirac cone on the surface. *Nature physics*, 5(6):438, 2009.

[51] Jinsong Zhang, Cui-Zu Chang, Zuocheng Zhang, Jing Wen, Xiao Feng, Kang Li, Minhao Liu, Ke He, Lili Wang, Xi Chen, et al. Band structure engineering in $(Bi_{1-x}Sb_x)_2Te_3$ ternary topological insulators. *Nature communications*, 2:574, 2011.

[52] Chujun Zhao, Han Zhang, Xiang Qi, Yu Chen, Zhiteng Wang, Shuangchun Wen, and Dingyuan Tang. Ultra-short pulse generation by a topological insulator based saturable absorber. *Applied Physics Letters*, 101(21):211106, 2012.

[53] M Zwiebler, JE Hamann-Borrero, M Vafaee, P Komissinskiy, S Macke, R Sutarto, F He, B Büchner, GA Sawatzky, L Alff, et al. Electronic depth profiles with atomic layer resolution from resonant soft x-ray reflectivity. *New Journal of Physics*, 17(8):083046, 2015.

APPENDICES

Appendix A

Drawing of In-situ Wiring Model

In Fig.A.1, there is a model of in-situ wiring device, consisting of a sample plate POGO pin connector and a receptacle 4-channel electrode connector. For the POGO pin connector, it is installed on the back side of the sample plate, which can make a connection with sample by adding insulated cap wires from backsides of pins. The pin heads can contact with electrodes in the sample receptacle add on piece as the sample plate is tightened by the side screw. All the grey parts shown in the figure are made by PEEK get from McMaster Carr, and the spring load POGO pin 5949T63, with an overall length of 0.66" and a 0.04" diameter, from the same supplier. Besides, two types of standard core wire (32 AWG and a slightly thicker 30 AWG) with kapton insulates are required for both sample connections and electrode connection. They are available at Accu-Glass company.

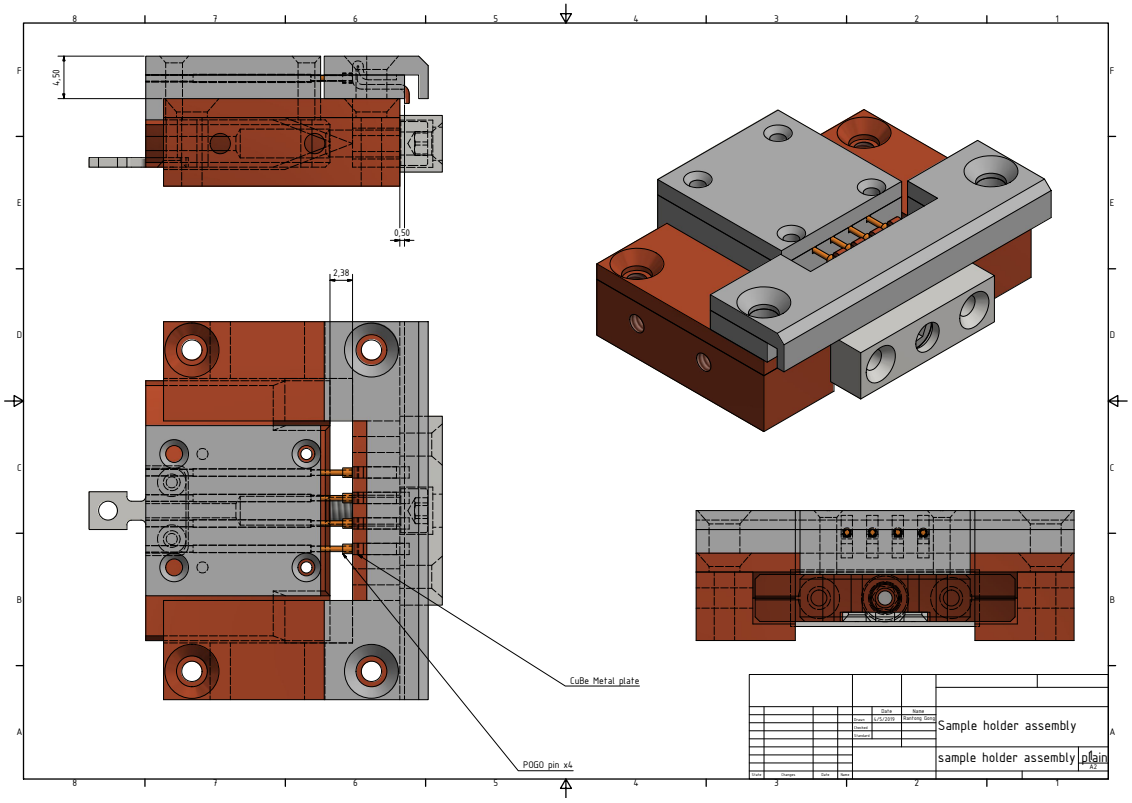

Figure A.1: Scheme of in-situ wiring device